UNIVERSITÀ
DI PAVIA

Dipartimento di Fisica

Corso di laurea magistrale in Scienze fisiche

Assessment of brain magnetic resonance spectroscopy (MRS): impact of physical parameters and coils on data quantification

Tesi per la laurea di:
Bianca Brancatelli

Relatrice:
Prof. Claudia Gandini

Correlatori:
Prof. Alessandro Lascialfari
Dr. Bhavana Solanky

Anno accademico 2025 – 2026

Contents

List of Figures

List of Tables

Abstract

Brain neurotransmitters act as vital chemical messengers between neurons, driving both physiological and cognitive processes. Magnetic Resonance Spectroscopy (MRS) is the only non-invasive technique capable of measuring localised concentrations of neurometabolites in vivo. By detecting the difference in resonant frequencies of protons (1H) between water and distinct molecules, determined by their local chemical environment, metabolic information can be simultaneously extracted from the resulting spectrum. The area under each spectral peak is proportional to the number of signal-generating protons, enabling concentration quantification within a volume of interest (VOI). Magnetic Resonance Spectroscopic Imaging (MRSI) extends this capability by generating spatial metabolic maps; however, its routine clinical application is hindered by low signal-to-noise ratio (SNR), lengthy acquisition times, and a lack of standardised protocols.

This thesis addresses the need to evaluate and optimise acquisition protocols and scanning parameters for 2D metabolic acquisition, enabling the accurate measurement of brain neurotransmitters within a clinically acceptable timeframe (e.g. <5-7 mins). The optimised protocol is subsequently applied to evaluate radiofrequency coil performance in measuring neurotransmitter concentrations, comparing a dedicated 1H multi-channel head coil against the 1H channel of a dual-tuned 1H/23Na coil.

To achieve these aims, the study was divided into three parts, with all scans performed on a Philips Ingenia CX 3T scanner. Firstly, in a phantom study scanning parameters (as water suppression, shimming and TR, SENSE and NSA) were systematically modified to optimise the acquisition of 2D Chemical Shift Imaging (CSI) slices using a Point Resolved Spectroscopy (PRESS) sequence and a General Electric GE-MRS "Braino" phantom. Secondly, the same scanner parameters were evaluated in vivo across four healthy controls (HCs), with the VOI positioned in cerebral white matter (WM). Thirdly, in vivo coil performance was evaluated by acquiring a single slice positioned within white matter using a PRESS sequence across five HCs, comparing the 32-channel head coil directly against the single-channel dual-tuned head coil.

Data preprocessing and spectral fitting were performed using TARQUIN software. Voxel-wise SNR and N-acetylaspartate (NAA) concentration maps were generated. While SNR across the VOI served as the primary comparison metric, NAA fitting accuracy (%SD $<$ 20) and the resulting NAA concentration estimates were evaluated as secondary parameters. Statistically significant differences ($p<0.05$) identified the optimal parameter configurations. For in vivo acquisitions, tissue segmentation from 3D T1-weighted images was performed to allow linear regression between WM fraction and NAA concentration to estimate metabolite levels in pure WM voxels.
Phantom optimisation demonstrated that disabling SENSE acceleration together with manual shimming volume selection yielded the highest SNR improvement. While setting SENSE to OFF doubled scan duration (from 1:22 min to 2:43 min in phantom, corresponding to 6:43 min in vivo), acquisition times remained clinically feasible for single-slice 2D acquisitions. In vivo evaluations confirmed that the 32-channel head coil significantly outperformed the dual-tuned coil in terms of SNR (mean SNR: 25.5±3.9 a.u. vs. 11.1±3.2 a.u., $p<0.05$), while retaining the capacity for parallel imaging acceleration when scan duration is prioritised. These optimised settings lay the groundwork for future investigations focusing on spatial resolution, 3D spectroscopic imaging, and applications targeting specific low-concentration metabolites.

I neurotrasmettitori cerebrali agiscono come messaggeri chimici tra neuroni, guidando processi fisiologici e cognitivi. La spettroscopia a risonanza magnetica(MRS) è l'unica tecnica non invasiva in grado di misurare le concentrazioni localizzate di neuro-metaboliti in vivo. Rilevando le frequenze di risonanza dei protoni(1H) nell'acqua e nelle diverse molecole, che variano leggermente in base al loro ambiente chimico locale, è possibile estrarre queste informazioni dallo spettro risultante: l'area sottesa a ciascun picco è proporzionale al numero di protoni generanti il segnale, consentendo la quantificazione della concentrazione molecolare nel volume di interesse(VOI). L'imaging spettroscopico (MRSI) estende questa misura generando mappe metaboliche spaziali; tuttavia la sua applicazione clinica è ostacolata da un basso rapporto segnale-rumore(SNR), da lunghi tempi di acquisizione e dalla mancanza di protocolli standardizzati.
Questa tesi risponde alla necessità di ottimizzare i protocolli di acquisizione e i parametri di scansione per l'MRSI 2D, permettendo la misurazione dei neurotrasmettitori entro tempi clinicamente accettabili(<5-7min). Questo protocollo ottimizzato è stato successivamente applicato per valutare le prestazioni di bobine a radiofrequenza nella misurazione, confrontando una bobina per

la testa multicanale dedicata all' 1H con il canale singolo 1H di una bobina dual-tuned 1H/23Na.
Per raggiungere questi obiettivi lo studio è stato suddiviso in tre parti, eseguendo le scansioni su uno scanner Philips Ingenia CX 3T. In prima fase, i parametri di scansione(quali la soppressione dell'acqua, lo shimming, il TR, il SENSE e il NSA) sono stati variati sistematicamente per ottimizzare l'acquisizione di strati 2D MRSI, usando la sequenza Point Resolved Spectroscopy(PRESS) su un fantoccio General Electric GE-MRS "Braino". Secondariamente gli stessi parametri sono stati affinati in vivo su quattro controlli sani(HC), con il VOI posizionato nella sostanza bianca cerebrale. Infine le prestazioni delle bobine sono state studiate acquisendo una singola fetta posizionata all'interno della WM mediante la sequenza PRESS su cinque HC, confrontando direttamente la bobina per la testa a 32 canali con la bobina per la testa a singolo canale.
Il pre-processamento dei dati e il fitting spettrale sono stati eseguiti usando il software TARQUIN, da cui sono state generate mappe rappresentanti l'SNR e la concentrazione di N-acetil aspartato(NAA) in ogni voxel. L'SNR all'interno del VOI ha rappresentato la metrica primaria di confronto, mentre l'accuratezza del fitting dell' NAA(%SD<20) e le stime di concentrazione sono state valutate come parametri secondari. Differenze statistiche significative($p<0,05$) tra le acquisizioni hanno consentito di identificare la configurazione ottimale di parametri. Per le acquisizioni in vivo, è stata eseguita la segmentazione tissutale a partire da immagini 3D pesate T1, per consentire la regressione lineare tra la frazione di WM e la concentrazione di NAA, al fine di stimare il livello di NAA in voxel di WM pura.
L'ottimizzazione su fantoccio ha dimostrato che la disattivazione dell'accelerazione SENSE, con la selezione manuale del volume di shimming, ha prodotto il miglioramento più significativo in termini dell'SNR. Nonostante impostare SENSE su OFF raddoppi la durata della scansione(da 1:22min a 2:43min sul fantoccio, corrispondenti a 6:43min di acquisizione in vivo), il tempo di acquisizione rimane clinicamente accettabile. Le valutazioni in vivo hanno confermato che la bobina per la testa a 32 canali supera nettamente la bobina dual-tuned in termini di SNR(SNR medio: 25,5±3,9a.u. vs. 11,1±3,2a.u., $p<0.05$), avendo la possibilità di accelerazione tramite imaging parallelo se necessario prioritizzare la durata dello scan. Questo lavoro pone le basi per indagini incentrate sulla spettroscopia 3D e su applicazioni dedicate a metaboliti a bassa concentrazione.

Chapter 1

Introduction

Brain neurotransmitters act as vital chemical messengers between neurons, driving both physiological and cognitive processes. Within the central nervous system, glutamate (Glu) serves as the primary excitatory neurotransmitter, with concentrations ranging from 5 to 15 mM, while gamma-aminobutyric acid (GABA), the major inhibitory neurotransmitter, reaches in vivo levels of only 1 to 2 mM. Both Glu and GABA play a crucial role in healthy brain function and are essential biomarkers for monitoring neurodevelopment as well as a wide spectrum of neurological disorders (such as Multiple Sclerosis, Alzheimer's disease, Parkinson's disease, and epilepsy) and psychiatric conditions (including anxiety, major depressive disorder, bipolar disorder, and schizophrenia) [4]. Hence, there is a strong interest in the neuroscience and neuropsychiatric communities in measuring the in vivo levels of these neurotransmitters [5].

Magnetic resonance imaging (MRI) technologies are particularly suitable for clinical trials as they are non-invasive, radiation-free, repeatable and widely available, but are not sensitive to physiological properties of the brain. Magnetic Resonance Spectroscopy (MRS) is the only non-invasive technique available to measure local concentrations of neurometabolites such as GABA and Glu in the brain. To evaluate metabolites, MRS detects the resonance of protons in water and other distinct molecules, which exhibit slight shifts in resonance frequencies due to their local molecular configuration: metabolites information can be extracted simultaneously from a spectra of normal brain, as shown in Figure 1.1 . On a state-of-the-art MR system, up to 15–20 different metabolites can be extracted simultaneously from a spectra [1], including N-acetylaspartate (NAA), creatine (Cr), choline (Cho), myo-inositol (mI), GABA and the combined signal of glutamate and glutamine (Glx) [6].
The areas under the different peaks of an MRS spectrum are proportional to the number of signal-generating protons in these molecules and consequently

allow for a concentration evaluation of the molecules in the volume of interest (VOI). While MRS is typically performed as single voxel spectroscopy, i.e. it selects a single areas in the brain from which the spectrum is recorded, MR Spectroscopic Imaging (MRSI) provides metabolic maps indicating the regional concentrations of different molecules [7].

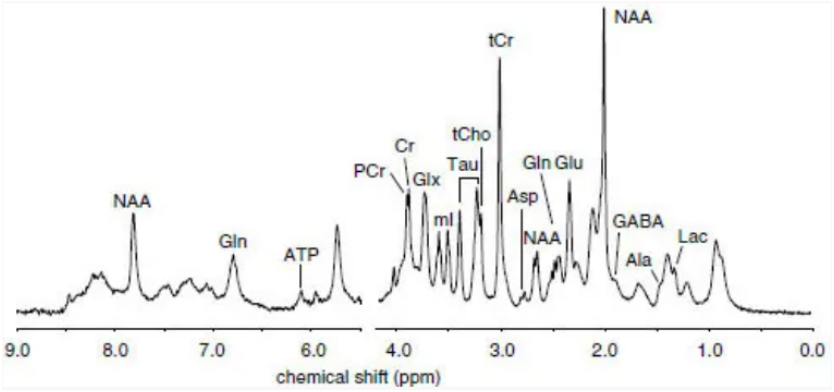

Figure 1.1: Nuclear magnetic resonance spectrum obtained from a rat brain in vivo [1]: on the x axis the chemical shift of each metabolite in parts per million (ppm), characteristic of different molecular environments. Concentration of each metabolites (as NAA, Glx, Cho, Cr, Lac) is the area under the related peak.

Despite the fact that MRSI provides valuable complementary information compared to conventional MRI, it is still not widely used in clinical practice. Major limitations include: (a) low signal-to-noise ratio, (b) poor spatial resolution, (c) prolonged acquisition times, (d) lack of standardized protocols, and (e) limited quality control. Since metabolite concentrations are very low, large voxel sizes are required to capture sufficient signal, resulting in low spatial resolution (typically around 1 cm^3). Additionally, high-spatial-resolution MRSI cannot be routinely acquired using standard clinical sequences because it requires long scanning times (e.g., in the range of tens of minutes) [8].
This thesis work stems from the need to evaluate optimized protocols and scanning parameters for 2D metabolic acquisitions, enabling accurate measurement of brain neurotransmitters within a clinically acceptable timeframe, a crucial factor for applications in MS and other conditions.

In the context of MRSI applied to MS, the study of regional GABA and Glutamate (Glu) alterations within lesions is ideally combined with the assessment of local sodium (23Na) concentration changes. In order to assess both sodium

and metabolite concentrations, it is necessary to use receiver coils sensitive to both ^{23}Na and ^{1}H. Within this research context, this thesis addresses the need to evaluate 1) sequence parameters for a clinically-feasible protocol and 2) the coil performance in measuring neurotransmitter concentrations, comparing a dedicated state-of-the art ^{1}H multi-channel head coil against the single channel ^{1}H coil of a dual-tuned ^{1}H/^{23}Na coil.

Chapter 2

Magnetic Resonance Spectroscopy Imaging

MRSI is a non-invasive technique that allows the study of molecular composition and the quantification of metabolite concentrations in the VOI, leveraging the physical principles of Nuclear Magnetic Resonance (NMR) combined with spatial localization techniques from Magnetic Resonance Imaging (MRI).

2.1 Nuclear Magnetic Resonance (NMR)

To understand MRI and subsequently MRSI, it is necessary to have an accurate knowledge of the physical phenomenon underlying these imaging and diagnostic techniques, known as NMR.
Nuclear Magnetic Resonance involves nuclei with an angular momentum I different from zero, an external magnetic field B_0, and a radiofrequency electromagnetic field B_1 resonating with the nuclei of interest.

In a classical description of atomic physics, nuclei with angular momentum (or nuclear spin) are viewed as rotating charged particles, consequently having an associated magnetic moment according to the equation

$$\vec{\mu_I} = \gamma \cdot \vec{I} \tag{2.1}$$

where $\vec{\mu_I}$ is the magnetic moment, $\vec{I}$ is the angular momentum, and γ is the gyromagnetic ratio, a parameter characterizing each nucleus.
It is the magnetic moment of the nuclei that interacts with the external magnetic field: each spin in the magnetic field experiences a torque, described by the equation

$$\vec{N} = \vec{\mu}_I \times \vec{B}_0 \tag{2.2}$$

that causes the spin to precess around the direction of the field, ultimately leading to a net alignment due to thermal interactions.

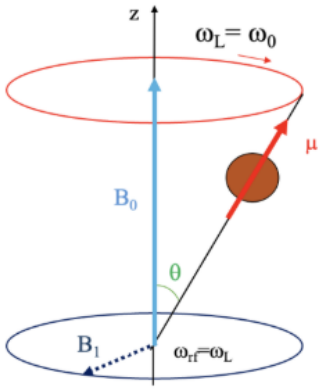

Figure 2.1: Spin motion due to the torque caused by the field B_0. A perpendicular electromagnetic field B_1, oscillating at the Larmor frequency, can be applied to increase the angle θ between the magnetic moment μ ant the main field B_0

Considering the torque and the conservation of angular momentum, assuming a spin that is not yet completely aligned with the external magnetic field, it will start to precess around the field, as shown in the Figure 2.1. This type of motion is described by the equation:

$$\frac{d\vec{\mu}_I}{dt} = \gamma\vec{\mu}_I \times \vec{B}_0 \tag{2.3}$$

From this relation, it is easy to identify the Larmor frequency

$$\omega_L = -\gamma B_0 \tag{2.4}$$

as the angular frequency of this motion, which occurs in a clockwise direction (hence the minus sign). The Larmor frequency is of fundamental importance in the description of Nuclear Magnetic Resonance.

Keeping the simplified description of a single nucleus in a classical physics approach, it is possible to understand the effect of the second applied field, the radiofrequency (RF) field $\vec{B}_1$, on this system. The RF field is generated perpendicularly to field $\vec{B}_0$ (which we can assume to be along the z-axis); it is an oscillating electomagnetic field characterized by the frequency ω_{rf} and can be seen as the sum of two rotating components, with the analytical expression:

$$\vec{B}_1 = B_1[\cos(\omega_{rf} \cdot t)\hat{x} + \sin(\omega_{rf} \cdot t)\hat{y}] \tag{2.5}$$

While the component rotating in the opposite direction with respect to the spin can be demonstrated to have no effect on the spin motion, the other is extremely efficient in tilting the nuclear magnetic moment into the plane in which it is rotating (the $\hat{xy}$ plane in our description) if the frequency characterizing the field is equal to the Larmor frequency of the nucleus involved (hence, if $\omega_{rf} = \omega_L$).
To understand why this tilting happens, the changes in the equation of motion should be studied, taking into account the equation in a rotating frame of reference. The new equation of motion, applying both $\vec{B}_1$ and $\vec{B}_0$, is:

$$\frac{d\vec{\mu}_I}{dt} = \gamma\vec{\mu}_I \times (\vec{B}_0 + \vec{B}_1) \tag{2.6}$$

It can be demonstrated that under the resonance condition ($\omega_{rf} = \omega_L$) and within a frame of reference rotating at the same frequency Ω ($\Omega = \omega_{rf} = \omega_L$), the equation simplifies to:

$$\frac{d\vec{\mu}_I}{dt} = \gamma\vec{\mu}_I \times \vec{B}_1 \tag{2.7}$$

This equation correctly describes a flipping of the spin towards the transverse plane, a flip described by the angle:

$$\Delta\theta = \gamma B_1 \cdot \Delta t \tag{2.8}$$

With Δt being the time interval in which the RF field $\vec{B}_1$ is turned on, what can be measured is the resulting flipping of the spin towards the plane in which $\vec{B}_1$ is rotating.

Applying the two magnetic fields to a real system (analyzing the effect on multiple spins), what is measured is the macroscopic nuclear magnetization $\vec{M}$. The latter is defined as the net magnetic moment per unit volume:

$$\vec{M} = \frac{1}{V}\sum\vec{\mu} \tag{2.9}$$

When the $\vec{B}_0$ field is applied to the sample, due to magnetic forces, a net nuclear magnetization of the sample is found to be aligned in the same direction as the external field.
Applying an RF field $\vec{B}_1$, the magnetization is then tilted, just as the individual magnetic moment of the atoms in the sample (specifically, those whose Larmor frequency equals ω_{rf}, thus satisfying the resonance condition with the applied RF field).

2.1.1 Quantum description

According to the quantization of angular momentum, energy can assume only discrete values. When an external magnetic field B_0 is applied to atoms with $I \neq 0$, the Zeeman splitting of the energy levels is observed, resulting in different energy states depending on the spin value:

$$E_m = -\gamma \cdot m_I \cdot \hbar \cdot B_0 \tag{2.10}$$

The proton spin angular momentum I can take on two orientations with respect to the external magnetic field, labeled as $m_I = \frac{1}{2}$ and $m_I = -\frac{1}{2}$, thus yielding two different energy levels (Figure 2.2). To minimize energy, the lower energy state becomes more populated according to the Maxwell-Boltzmann distribution:

$$P_+ = \frac{\exp(-\frac{E_+}{k_B \cdot T})}{\exp(-\frac{E_+}{k_B \cdot T}) + \exp(-\frac{E_-}{k_B \cdot T})} \tag{2.11}$$

$$P_- = \frac{\exp(-\frac{E_-}{k_B \cdot T})}{\exp(-\frac{E_+}{k_B \cdot T}) + \exp(-\frac{E_-}{k_B \cdot T})} \tag{2.12}$$

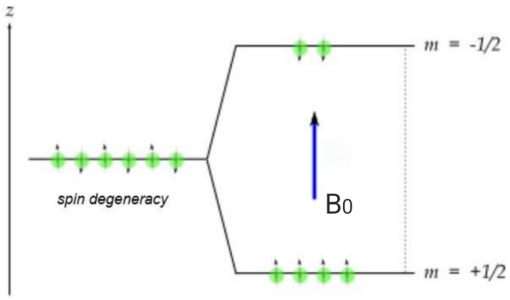

Figure 2.2: Distribution of the spins in the energy levels caused by Zeeman splitting

Where k_B is the Boltzmann constant and T is the temperature of the sample. From the distribution of the atomic population across the two energy levels, a net macroscopic magnetization M_0 can be derived, measured as:

$$M_0 = \frac{N \cdot \mu_I^2}{V \cdot k_B \cdot T} \cdot B_0 \tag{2.13}$$

2.1.2 Bloch equations

What was observed in NMR experiments is that the equation of motion described until now is, in fact, incomplete: after the tilting of the magnetization into the transverse plane, two relaxation processes of the magnetization were observed, as the signal registered by the coil was found to decay over time. To complete the description of the system, the Bloch equations were derived from a phenomenological point of view.

The idea behind the Bloch equations is that the two components of the magnetization decay in different ways. After a perturbation, M_z returns to its equilibrium position due to the continuous presence of the main field $\vec{B}_0$. This phenomenon is described by the spin-lattice relaxation time T_1, which dictates how fast M_z returns to its equilibrium value M_0. It is named after the energy exchange between the spins and the surrounding environment (the lattice) that causes the relaxation of M_z back to equilibrium. The complete equation of motion for M_z, after the perturbation, is:

$$\frac{dM_z}{dt} = \gamma(\vec{M} \times \vec{B}_0)_z + \frac{1}{T_1}(M_0 - M_z) \tag{2.14}$$

The time evolution of M_{xy}, is instead mainly due to another effect, characterized by the spin-spin relaxation time T_2. The T_2 time describes the disappearance of the transverse magnetization M_{xy} due to interactions between different spins: each nucleus experiences a local magnetic field at its specific position that is slightly different from $\vec{B}_0$, owing to the local fields of the surrounding nuclei. This variation in the field causes a distribution in the frequencies at which the spins precess in the plane (the Larmor frequency, as described by the equation (4)). As a result, the spins get dephased over time, causing the total transverse magnetization M_{xy} to decay to zero, as described by the equation:

$$\frac{dM_{x/y}}{dt} = \gamma(\vec{M} \times \vec{B}_0)_{x/y} - \frac{M_{x/y}}{T_2} \tag{2.15}$$

Since the differences in the magnetic field in different positions are caused not only by local spin-spin interactions but also by spatial inhomogeneities in the main field $\vec{B}_0$, it is necessary to define an effective relaxation time T_2^* as:

$$\frac{1}{T_2^*} = \frac{1}{T_2} + \frac{1}{T_2'} \tag{2.16}$$

where T_2 describes how fast M_{xy} disappears due to field variations caused by spin-spin interactions, T_2' describes the decay of M_{xy} due to the inhomogeneity

of the external field, and T_2^* is the total time coefficient taking both phenomena into account.

Equations 2.14 and 2.15 are the Bloch equations. In NMR experiments, after a $\frac{\pi}{2}$ pulse (meaning an RF pulse after which the magnetization is correctly flipped into the transverse plane, so that $\Delta\theta = \frac{\pi}{2}$, from the Equation 2.8) the Bloch equations can be solved as:

$$M_z(t) = M_0 \cdot \left(1 - e^{-\frac{t}{T_1}}\right) \tag{2.17}$$

$$M_{xy}(t) = M_0 \cdot e^{-\frac{t}{T_2^*}} \tag{2.18}$$

The behavior of the magnetization over time after a $\frac{\pi}{2}$ pulse is shown in Figure 2.3, and it is confirmed by NMR experimental data.

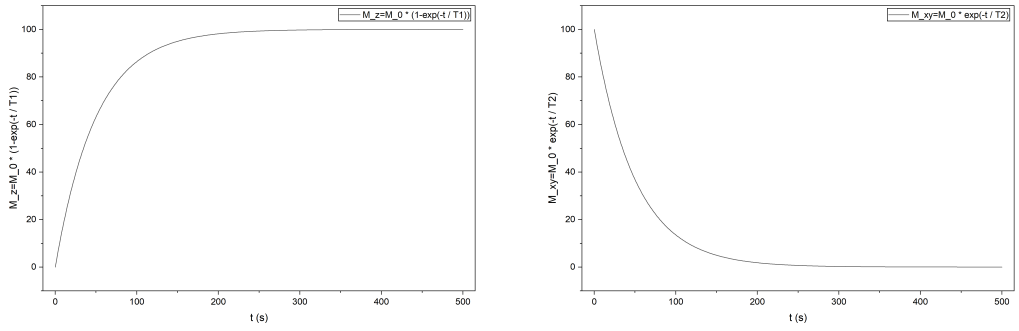

Figure 2.3: M_z recovery and M_{xy} decay after a $\frac{\pi}{2}$ RF pulse

2.1.3 Signal and sequences

The aim of NMR experiments in most applications is to tilt the spins of Hydrogen nuclei (^{1}H), for which the gyromagnetic ratio divided by 2π ($\gamma/2\pi$) is equal to 42,58 MHz/T. This phenomenon is exploited to obtain information (e.g., regarding the composition) of the system under evaluation.
In a typical NMR experimental setup, the external magnetic field is generated along the $\hat{z}$ direction by a magnet or a superconducting coil. During the experiment, the sample remains fixed within the $\vec{B}_0$ field, while the $\vec{B}_1$ RF field is applied to the sample via a secondary coil with its axis in the $\hat{xy}$ plane. In this second coil, a pulse of alternating current creates an oscillating magnetic field, which acts on the sample for a time interval Δt equal to the pulse duration. The field $\vec{B}_1$ is thus created rotating in the $\hat{xy}$ plane, tilting the magnetization along the θ direction as shown in Figure 2.1.

The same coil used to transmit the RF field is then used to acquire the signal: if the magnetization is correctly tilted into the transverse plane where the coil is positioned, the magnetization, which continuously rotates around $\vec{B}_0$ (as described by Equation 3), induces an alternating current in the coil, which is then measured as the NMR signal.
Due to the effects described by the Bloch equations, the signal measured by the coil is not constant over time; it oscillates at the Larmor frequency and decays exponentially, reflecting the decay of M_{xy} expressed in Eq. (2.18). The signal recorded immediately after a $\frac{\pi}{2}$ pulse is known as the Free Induction Decay (FID), and it can be described by Figure 2.4 and the following formula:

$$s(t) \propto \omega_L \cdot V_{\text{sample}} \cdot M_{xy}(0) \cdot \exp\left(-\frac{t}{T_2^*}\right) \cdot \exp(-i\omega_L t) \tag{2.19}$$

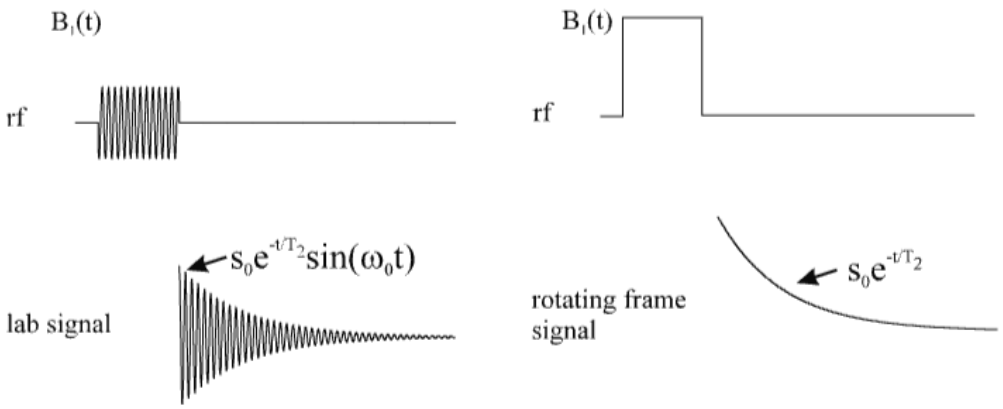

Figure 2.4: Free Induction Decay (FID) signal acquired in laboratory frame and rotating frame of reference for spins rotating at the same Larmor Frequency [2]

A more common and practical sequence involves two pulses: the first is a 90-degree pulse that flips the magnetization into the transverse plane where the coil is located, while the second is a 180-degree pulse that refocuses the magnetic field inhomogeneities, allowing the true T_2 of the system to be measured. This procedure is called the Spin-Echo (SE) sequence, as depicted in Figure 2.5. The core concept is to acquire the signal at the peak of the echo, when all spins are back in phase, and systematically vary the Echo Time (TE, time at which the echo signal appears) to reconstruct the T_2 decay curve.

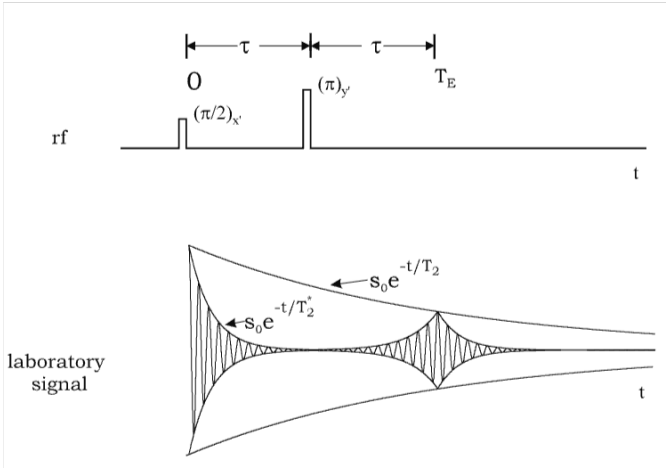

Figure 2.5: Spin Echo foramtion: A $\frac{\pi}{2}$ pulse followed by a π pulse applied at time τ to invert the accumulated phase and acquire an Echo signal at time TE (echo time) $= 2\ \tau$[2]

By acquiring the signal as a function of time, it is possible to transition to the frequency domain through the Fourier Transform (FT). This allows for the monitoring of the Larmor frequency distribution that composes the NMR signal, as described by Eq. (2.20). The result of this operation is a Lorentzian function centered at the specific Larmor frequency, which reflects the precession of the nuclear spins within the sample.

$$f(\omega) = \int_{-\infty}^{+\infty} s(t) \cdot \exp(-i\omega t), dt \tag{2.20}$$

2.2 Magnetic Resonance Imaging (MRI)

MRI is an application of NMR principles that provides spatially localized information about a body (typically in the form of an image), based on the magnetic properties of the nuclei. It provides a matrix of voxels where information about the proton density, T_1, or T_2 of the matter is stored and represented in grayscale. It is a non-invasive imaging method that allows for the representation of body slices, creating sagittal, coronal, and axial images. In MRI, spatial encoding is achieved using linear magnetic field gradients, overlapping with the static and uniform magnetic field, and defined as:

$$G_x = \frac{\partial B_z}{\partial x}, \qquad G_y = \frac{\partial B_z}{\partial y}, \qquad G_z = \frac{\partial B_z}{\partial z} \tag{2.21}$$

In the 1D case, how the resonance frequency becomes site-dependent can be easily explained with the formulas:

$$B_z = B_0 + G_x x \qquad \omega(x) = \omega_0 + \gamma G_x x \tag{2.22}$$

As this equation suggests, by applying a gradient, a distribution of resonance frequencies can be observed that increases along the x-axis. By selecting the frequency $\omega(x')$ of the radiofrequency pulse, only the protons positioned at x' are excited, providing spatially localized information.
In a 3D acquisition, this process is called slice selection: if the gradient is applied along x, we excite all the protons positioned in a sagittal slice (located at x'). If the gradient is applied along y or z, the image created will be coronal or axial, respectively.
To spatially localize information within the slice, a subsequent step called k-space encoding is required.

2.2.1 Signal and k-space encoding

Similarly to the NMR signal, the signal acquired by the coil during MRI acquisition can be written as:

$$s(t) = \int d^3r \cdot \rho(\vec{r}) e^{i\phi(\vec{r},t)} \tag{2.23}$$

where $\rho(\vec{r})$ is the effective spin density at position r and $\phi(\vec{r},t)$ is the accumulated phase up to time t, related to the applied gradient $\vec{G}$:

$$\phi(\vec{r},t) = -\int_0^t dt' \omega_G(\vec{r},t') = -\gamma \vec{r} \cdot \int_0^t dt' \vec{G}(t') \tag{2.24}$$

Defining the spatial frequency $\vec{k}$ as:

$$k_x(t) = \frac{\gamma}{2\pi}\int_0^t dt' G_x(t'), \quad k_y(t) = \frac{\gamma}{2\pi}\int_0^t dt' G_y(t'), \quad k_z(t) = \frac{\gamma}{2\pi}\int_0^t dt' G_z(t') \tag{2.25}$$

the proton density can be easily identified as the Fourier transform pair of the MRI signal written as a function of $\vec{k}$:

$$\rho(\vec{r}) = \int d^3k \cdot s(\vec{k}) e^{i2\pi\vec{k}\cdot\vec{r}} \tag{2.26}$$

Consequently, in MRI, the image space ($\vec{r}$) is connected to the data space ($\vec{k}$), and the image is reconstructed through a process called k-space coverage/encoding, where the signal is acquired over a sufficient range of k-values.

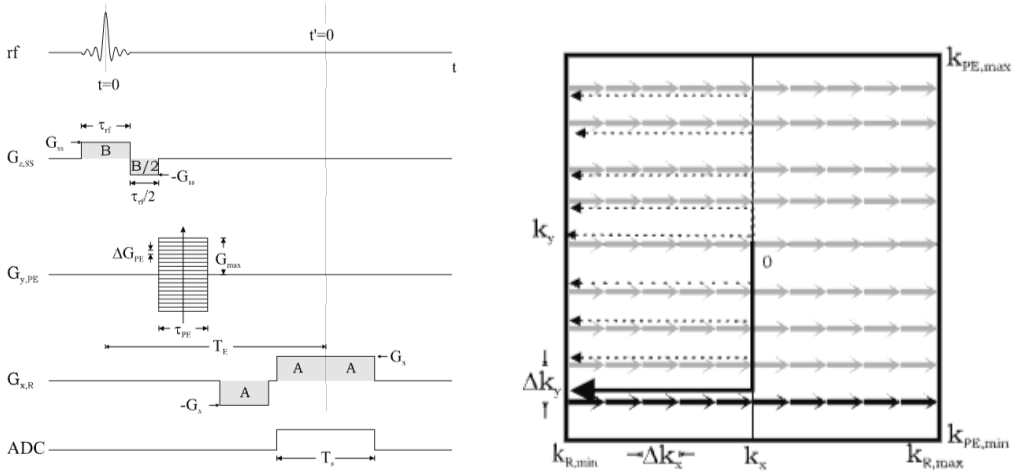

(a) Rf impulse and applied gradient (b) Resulting k-space coverage

Figure 2.6: D Gradient Echo acquisition showing (a) the RF pulse and applied gradients, and (b) the corresponding trajectory in k-space. RF: radiofrequency pulses; G_z, G_x, and G_y: slice-selection, phase-encoding, and spatial-encoding gradients, respectively; ADC: analog-to-digital conversion window for signal acquisition.

As shown in Figure 2.6, the MRI image can thus be reconstructed by acquiring sufficient signal in k-space. The slice selection is performed as described in Equation 2.22 by applying a gradient (along the z-direction in the figure), which is called the Slice Selection (SS) Gradient. Then, a second gradient, called the Phase Encoding (PE) Gradient, is applied along another direction (y-direction in the image): it selects k_y values in k-space, allowing the sampling of the signal along that line. If the gradient is constant over time, the selected k_y value is easily described by the equation:

$$k_y = \frac{\gamma}{2\pi} G_y t \tag{2.27}$$

To acquire multiple lines positioned at different k_y values, the sequence is repeated by applying a PE gradient at different intensities, resulting in Δk_y steps:

$$\Delta k_y = \frac{\gamma}{2\pi} \Delta G_y t \tag{2.28}$$

The third gradient in the figure, applied along the x-direction, is called the Readout (RO) Gradient and allows movement horizontally in k-space, as k_x follows the equation over time:

$$k_x(t) = \frac{\gamma}{2\pi} G_x t \tag{2.29}$$

It is while this gradient is turned ON that data collection takes place.

2.2.2 Echo and Repetition Times

MRI image acquisition is described by two important adjustable parameters: Echo Time (TE) and Repetition Time (TR).
TE represents the time elapsed after the initial radiofrequency pulse at which signal acquisition is performed, while TR is the time interval between consecutive repetitions of the sequence. Because of relaxation processes, the sequence is usually repeated multiple times to enable complete k-space coverage.
Taking these two parameters into account, the MRI signal can also be written as:

$$s(t) \propto \rho \cdot \left(1 - e^{-\frac{TR}{T_1}}\right) \cdot e^{-\frac{TE}{T_2}} \tag{2.30}$$

By adjusting these parameters, it is thus possible to weight the image in different ways: T1-weighted (T1W), T2-weighted (T2W), or proton density-weighted (PDW), thereby accentuating or attenuating specific tissues based on their relaxation properties.

2.3 Magnetic Resonance Spectroscopy Imaging (MRSI)

MRSI extends conventional MRI acquisition by adding a spectral dimension, enabling the spatial mapping of biochemical metabolites in vivo. By acquiring localized NMR spectra across a volume, MRSI allows for the non-invasive quantification of tissue chemistry, thanks to the physical phenomena of Chemical Shift.

2.3.1 Chemical Shift

In NMR experiments, nuclei resonate under the effect of an external magnetic field at a specific frequency called the Larmor frequency, as described by Equation 2.4.
However, even when considering the signal from the same type of atom (typically hydrogen), the frequency at which it resonates varies depending on the

molecule to which it is bound. The molecular environment induces a magnetic shielding effect caused by surrounding electrons, leading to slightly different precession frequencies.
These frequency changes are expressed in terms of the "chemical shift" [2], where the shielding constant σ is defined as:

$$\sigma = \frac{B_{shifted} - B_0}{B_0} = \frac{\omega_{shifted} - \omega_0}{\omega_0} \tag{2.31}$$

To obtain a dimensionless quantity independent of the applied magnetic field, this frequency shift is usually expressed in parts per million (ppm).
As specified in Section 1.1.3 and Equation 2.20, the NMR signal in the time domain can be converted into a Lorentzian peak centered at the precession frequency using the Fourier Transform (FT). By applying a broadband RF pulse containing a wide range of frequencies, we can acquire a more complex FID or echo signal. Decomposing this signal via Fourier transform resolves the different molecules present, as each distinct chemical environment corresponds to a specific resonance frequency.
Once the spectrum is acquired, allowing Magnetic Resonance Spectroscopy (MRS), the concentration of each molecule can be determined from the area under its corresponding peak, since each nucleus contributes a fixed amount to the total signal intensity.

2.3.2 Chemical Shift Imaging (CSI)

CSI refers to the process of obtaining the spatial dstribution of identical nuclei that experience different levels of magnetic shielding due to their chemical environments. A chemical shift encoding axis can be defined in terms of σ, typically quoted in part per million (ppm). This creates an effective imaging axis, leading to a 3D or 4D space made up of three spatial dimensions and a spectral dimension σ. In the corresponding expression of the signal, the chemical shift phase effects are to be added to those due to applied gradients, leading to the generalization of the signal equation as the 4D FT:

$$s(\vec{k}, t) = \int d^3r d\sigma \rho(\vec{r}, \sigma) e^{-i(2\pi\vec{k}\cdot\vec{r} - \sigma\omega_0 t)} \tag{2.32}$$

In typical CSI, data are read along the time axis, having M_{xy} allowed to evolve in time under the influence of chemical shift: that means that each spatial axis is treated with PE gradients, used to locate a position in the k-space before the data are taken [2]. Consequently a line of chemical shift data is collected at a specific point in k-space during each repetition of the experiment, as shown in

Figure 2.7. The corresponding 2D-spatial, 1D-spectral representation is shown in Figure 2.8.
MRSI follows CSI, having the signal intensity of a single metabolite in each voxel, color encoded according to the concentration, to assest the distribution of a specific brain metabolite [9].

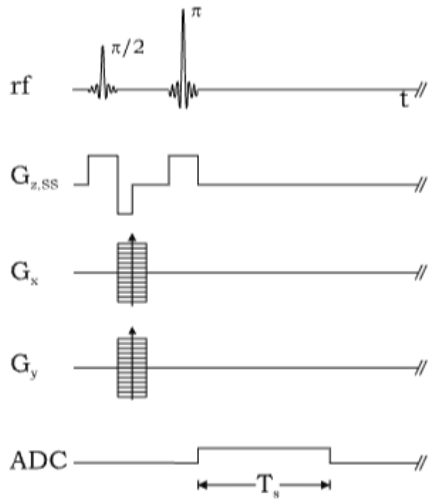

Figure 2.7: Pulse sequence diagram of a 2D spin-echo Chemical Shift Imaging (CSI) sequence [2]. RF: radiofrequency pulses; G_z, G_x, and G_y: slice-selection, phase-encoding, and spatial-encoding gradients, respectively; ADC: analog-to-digital conversion window for signal acquisition.

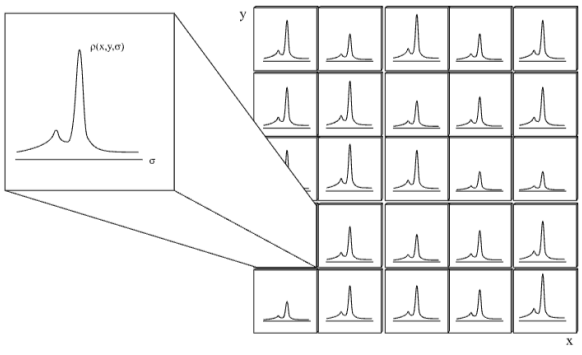

Figure 2.8: Chemical shift information represented in each voxel, spatially encoded by the gradients [2]

Chapter 3

Physical parameters and coils

To improve the quality of MRS/MRSI acquisitions, several physical parameters related to the sequence and scanner settings can be modified to achieve a higher signal-to-noise ratio (SNR) in a shorter acquisition time.
The aim of this thesis is to enhance MRS acquisition by studying the impact of these parameters, alongside the influence of coil selection. This section explains the physical and theoretical principles behind each parameter, using the terminology and settings standard to Philips scanners, as these were used for this work.

3.1 Scanner parameters

3.1.1 Field of View and Volume of interest

The MR signal is generally collected over a set of uniformly spaced points in k-space. Along the read direction, considering a constant read gradient G_R such sampling is achieved with Δk steps:

$$\Delta k = \frac{\gamma}{2\pi} G_R \Delta t \tag{3.1}$$

Doing the FT of the signal, the periodic Fourier series yields to an infinite set of exact copies of the information, provided that the period associated is larger than the interval outside wich the information ends [2].
This periodicity is given by the reciprocal of the spacing of the sampling function, thus:

$$\frac{1}{\Delta k} = L = FOV \tag{3.2}$$

where L is the spacial interval over wich the reconstructed image repeats itself: this interval L is called Field Of View (FOV).

If the FOV is too small, smaller than the object to be imaged the image wraps around, with the pixels near the edges of the FOV that are mapped inside L, creating an artifact called aliasing. To avoid this type of error, data must be sampled such that the FOV is larger than the object size, following the Nyquist sampling criterion [2]:

$$L > A \qquad or \qquad \Delta k < \frac{1}{A} \tag{3.3}$$

Inside the FOV another volume is defined: restricting signal detection to a well-defined VOI is crucial for meaningful in vivo NMR spectroscopy. First and foremost, spatial localization is used to remove unwanted signals from outside the VOI, like extracranial lipids in MRS applications of the brain. However, spatial localization has many additional beneficial effects, in particular in managing tissue and magnetic field heterogeneity. For example, at a macroscopic level the brain can be segmented into gray matter, white matter and CSF, each of which has unique metabolic profiles. Careful positioning of the localized volume can minimize 'partial volume effects' (i.e. contamination of signal from one compartment by signal from another compartment), thereby providing a more genuine tissue characterization.[1] Additional benefits of spatial localization originate from the fact that variations in B_0 and B_1 magnetic fields are greatly reduced over the small localized volume, thereby providing narrower spectral lines and more uniform signal excitation and reception, respectively. Spatial localization does not only allow the unambiguous detection of metabolites from a well-defined spatial volume, but also increases the spectral resolution by: (1) narrower resonances; (2) exclusion of broad unwanted resonances; and (3) improved water suppression [1].

3.1.2 Water suppression

The spectral width of the water resonance is several orders of magnitude larger than those of low-concentration metabolites, making metabolite detection difficult and ambiguous. As water is the most abundant compound in biological tissue, the proton NMR spectrum of almost all tissue is dominated by a resonance at 4,7 ppm originating from the two protons of water.
Suppression of the water signal is hence essential to enable reliable and consistent detection of metabolite spectra [1].Three types of water suppression (WS) have been studied: frequency-selective excitation (Excitation), CHEmical Shift Selective (CHESS) [10], and Multiply Optimized Insensitive Suppression Train (MOIST) water suppression.

- **Excitation** water suppression uses selective RF pulses, precisely shaped to match the metabolites' bandwidth (excluding the water frequency), to minimize the water signal at the start of acquisition [11].
- **CHESS** water suppression uses narrowband selective pulses, centered at 4,7 ppm, to tip water protons into the transverse plane, followed by spoiler gradients that rapidly dephase and remove the water signal.
- **MOIST** water suppression uses multiple phase-modulated RF pulses alongside spoiler gradients interspersed between pulses; the flip angle of each RF pulse is optimized to account for B_1 inhomogeneities, making MOIST highly robust against them [11].

3.1.3 TE/TR

As described in Section 2.2.2, adjusting the TE and TR parameters allows the MRI image to be weighted differently. The same principle applies to MRS: since different metabolites are characterized by distinct T_1 and T_2 relaxation times, selecting a short or long TE determines whether metabolites with a short T_2 are detectable. On the other hand, using a longer TR increases longitudinal recovery, meaning a higher signal from the metabolites at the cost of a longer acquisition time.

3.1.4 Shimming

In the presence of B_0 inhomogeneity, spins within the volume resonate at different Larmor frequencies ω_n. As a result, the individual Lorentzian lines are centered at different frequencies and thus do not add coherently. Instead, a broadened, non-Lorentzian resonance line is obtained, in which the frequencies are spread over a range dictated by ω_n.
If inhomogeneities are instead present in the B_1 field, spins are excited and refocused improperly due to flip angles θ that deviate from expected values, ultimately leading to a lower SNR.
The homogeneity of the applied magnetic field is thus an important characteristic of the scanner, however, the finite length of the superconducting coils generating the main magnetic field together with unavoidable manufacturing tolerances, inevitably leads to small deviations from ideal homogeneity.
For MRS studies, field homogeneity requirements are particularly stringent: for instance, a clear separation between the choline and total creatine resonances in ^{1}H-MRS requires a minimum magnetic field homogeneity of 0,1–0,2 ppm and achieving high spectral resolution and high SNR strictly necessitates

high magnetic field homogeneity.
To assess and guarantee B_0 homogeneity, modern magnets are equipped with shim coil which, on a subject-specific basis, accomplish Magnetic field homogeneity through active shimming.
The shimming process attempts to cancel the measured magnetic field deviation $\Delta B_0(x,y,z)$ mapped across the VOI, as expressed in the Equation 3.4:

$$\Delta B_0(x,y,z) = B_{0,\text{offset}} + \sum_{n=1}^{\infty}\sum_{m=0}^{n} C_{n,m}F_{n,m}(x,y,z) \tag{3.4}$$

The minimization procedure is a fully automated method: for in vivo shimming, the coefficients $C_{n,m}$ in Equation 3.4 are determined directly from magnetic field maps. Following the definition of a region of interest, the optimal shim currents are calculated via least-squares minimization by finding the coefficients $C_{n,m}$ that minimize [1]:

$$\left[B_{0,\text{offset}} + \sum_{n=1}^{\infty}\sum_{m=0}^{n} C_{n,m}F_{n,m}(x,y,z) - \Delta B_{0,\text{measured}}(x,y,z)\right]^2 \tag{3.5}$$

The scanner parameter designated as "Shimming" allows the user to select the region of interest where magnetic field homogeneity must be optimized. Selecting the "PB_auto" option automatically fits the shimming volume around the target VOI, whereas "PB_volume" allows for manual positioning and sizing of the shim volume.

3.1.5 SENSE (Sensitivity Encoding)

An approach to scan time reduction is provided by parallel imaging methods, which take advantage of the local spatial sensitivity information of an array of multiple receive elements of a multi-channel coil to partially replace spatial encoding by magnetic field gradients. Since signal can be acquired simultaneously (i.e. in parallel) by multiple receive coils, a reduction in k-space sampling directly results in a reduced image acquisition time while maintaining full spatial resolution. [1]
One of the most well known and commonly used parallel MRI techniques is SENSE (sensitivity encoding) [12]. Setting "SENSE" to ON at the scanner, the image scan time can be reduced e.g. fourfold by only acquiring every fourth line in k-space, which is equivalent to a fourfold reduction of the FOV in one direction. Signal outside of the reduced FOV will be sampled at an apparent lower frequency in order to satisfy the Nyquist sampling condition, described by the formula 3.3. As a result, signal from outside the reduced FOV is aliased

to within the FOV leading to a folded image. This image can be unambiguously unfolded with the aid of additional information about the spatial origins of the signal and parallel MRI methods provide the additional information through the spatially dependent sensitivity map of each element of a multi-channel RF coil. Being a parallel MRI method, signal from all elements of the multi-channel coil is acquired simultaneously, allowing an important reduction, e.g. 4 times, in scan time [1].

3.1.6 RF shape

RF pulse shape is relevant in NMR experiments as it enables a high degree of selectivity in the excited frequency range, which is defined by the pulse's sharpness. Beyond frequency selectivity, the pulse shape directly impacts the total acquisition time as well as the minimum selectable TE and TR: shorter pulses may sacrifice frequency profile sharpness, but they allow for shorter TE and TR values. The Philips scanner provides four selectable pulse shape options: Classic-short , Classic-long, Normal, and Sharp.

3.1.7 Saturation Bands

Excitation of subcutaneous lipids represents a major challenge in 3D brain MRSI, significantly limiting the achievable spatial coverage. Within the head, metabolites of clinical interest, such as choline, creatine, lactate, and N-acetyl-aspartate (NAA), exist at concentrations roughly 10^4 times smaller than those of water and subcutaneous lipids.
If subcutaneous lipids are excited, a severe artifact can contaminate voxels within brain tissue, as lipid excitation produces a prominent peak around $1,3$ ppm. For this reason, the rectangular VOI must be kept relatively small to avoid signal contamination from subcutaneous fat or cerebrospinal fluid (CSF).
Saturation bands (sat bands) are employed to further suppress lipid excitation caused by voxel bleeding (i.e., the unwanted excitation and signal leakage of protons from regions bordering the VOI). A sat band eliminates most of the MR signal within a defined spatial slab by applying frequency-selective RF suppression pulses in the presence of slice-selection gradients, followed by strong crusher gradients to dephase the excited transverse magnetization [13].
Sat bands can be positioned either manually or automatically by the scanner around the VOI. In addition to mitigating artifacts caused by voxel bleeding, they also prevent aliasing phenomena (described in Section 3.1.1) by dephasing and eliminating the signal originating from tissues outside the selected FOV.

3.1.8 Shift Direction

Due to the chemical shift effect, different metabolites resonate at slightly different Larmor frequencies. Since the MRI scanner localizes voxels using spatial magnetic field gradients, the RF pulse excites the prescribed voxel based on the resonance frequency of water. However, brain metabolites and lipids are excited at slightly shifted positions along the gradient axis. Consequently, the effective volume acquired for each metabolite is physically displaced from the nominal voxel location selected on the scanner, giving rise to the Chemical Shift Displacement Error.
By adjusting the "shift direction" parameter on the scanner interface, the operator can control the spatial axis along which this displacement occurs: options typically include Left-Right (LR) or Anterior-Posterior (AP), in the combinations Anterior-Left (AL), Anterior-Right (AR), Posterior-Left (PL) and Posterior-Right (PR). Strategic selection of the shift direction enables the displacement of unwanted lipid signals away from critical brain structures or directly into predefined saturation bands for effective suppression.

3.1.9 Number of Signal Averaged (NSA) and dynamic study

The NSA is the number of times each line in k-space is filled or sampled. Because it represents the number of times each line acquisition is repeated, it affects scan time, directly proportional to the NSA value selected. Increasing the number of averages enhances the SNR within each voxel of the reconstructed image [14].

Conversely, when the number of dynamic scans is set to a value greater than one, the sequence is repeated sequentially over time to enable dynamic temporal evaluation. Similar to NSA, the overall acquisition duration scales linearly with the number of selected dynamic phases.

3.2 Multi-channel coils

Constraints on total scan time and SNR represent primary considerations when designing MRSI protocols for clinical applications. The implementation of multi-channel phased-array receive coils effectively alleviates these limitations. However, it introduces new methodological challenges, particularly regarding the efficient combination of data from multiple receive channels and the requirement for a uniform B_1 transmit field to ensure homogenous proton excitation [15].

While a single-channel coil can only be optimized for a specific localized region, multi-channel coil arrays are meant to allow coverage of larger or multiple volumes without significantly sacrificing SNR and without extending acquisition time. To optimize the overall SNR from a given volume of interest, the relative amplitudes and phases of the signals detected by individual array elements must be appropriately adjusted prior to channel combination. Specifically, N independent signals are recorded and processed retrospectively using a set of voxel-specific weighting factors designed to maximize the array's combined SNR, as shown in Figure 3.1. The most common approach is the sum-of-squares (SoS) combination method, which operates under the assumption that the pixel intensity in each uncombined coil image serves as a reliable proxy for that channel's localized SNR [3].
Consequently, selecting an optimal reception coil for spectroscopic imaging involves evaluating key trade-offs between single-channel and multi-channel configurations. Superior sensitivity across varying tissue depths is achievable by replacing a large single-channel coil with an array of smaller coil elements spanning the same surface area, with the most pronounced SNR gains observed in regions closer to the coil elements. Initial studies demonstrate substantial potential for phased-array coils in MRSI, particularly within CSI frameworks [3].

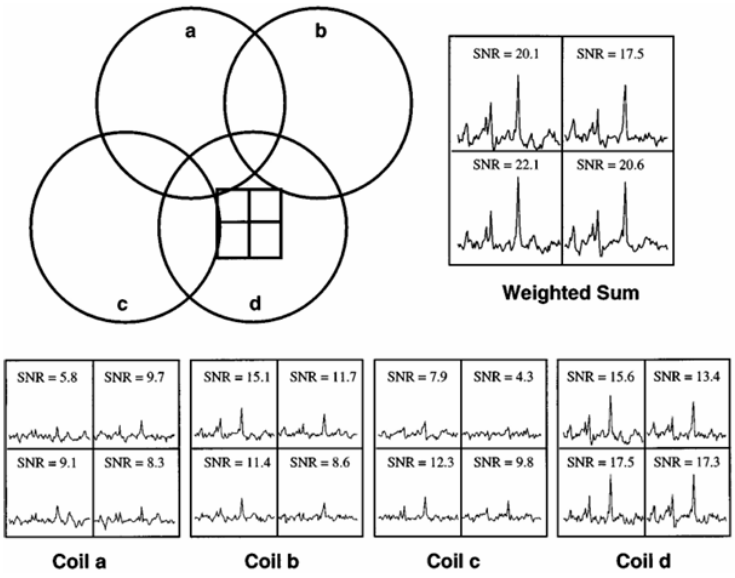

Figure 3.1: Combination of signal from different coils to improve SNR in a multi-channel coil set up [3]

Chapter 4

Materials and Methods

All scans were performed on a Philips Ingenia CX 3T MRI scanner using either a 32-channel ^{1}H or a single-channel $^{1}H/^{23}Na$ head coil.
The study was divided into three parts:

- Optimization of the scanner parameters described in Section 3.1 to acquire 2D CSI slices using a PRESS sequence [16] on a GE-MRS "Braino" phantom, using the 32-channel coil.
- Optimization of the scanner parameters in vivo on four healthy controls (HCs), acquiring 2D PRESS-CSI slices positioned in the white matter, using the 32-channel coil.
- Acquisition of a single slice positioned within white matter using a PRESS sequence in five HCs with both 32-channel and single-channel multinuclear head coils, to allow for a comparison of coil performance.

4.1 BRAINO and partecipants

The GE-MRS “Braino” phantom is a water based sphere containing N-acetyl-l-aspartic acid [NAA], 12,5 mM; creatine hydrate [Cr], 10 mM; choline chloride [Ch], 3 mM; myo-inositol [mI], 7,5 mM; l-glutamic acid [Glu], 12,5 mM; dl-lactic acid [Lac], 5 mM; sodium azide (0,1%); potassium phosphate monobasic [KH2PO4], 50 mM; sodium hydroxide [NaOH], 56 mM; and Gd-DPTA [Magnevist], 1 mL/L [17].

For the in vivo testing and the final study, eight healthy volunteers were recruited (5 females and 3 males). All volunteers gave informed consent according to a protocol approved by the UCL/UCLH ethics committee for Physics

development studies. Data were pseudo-anonymised and transferred to the NMR Research Unit, Queen Square Multiple Sclerosis Centre secure network for analysis.

4.2 Point RESolved Spectroscopy (PRESS)

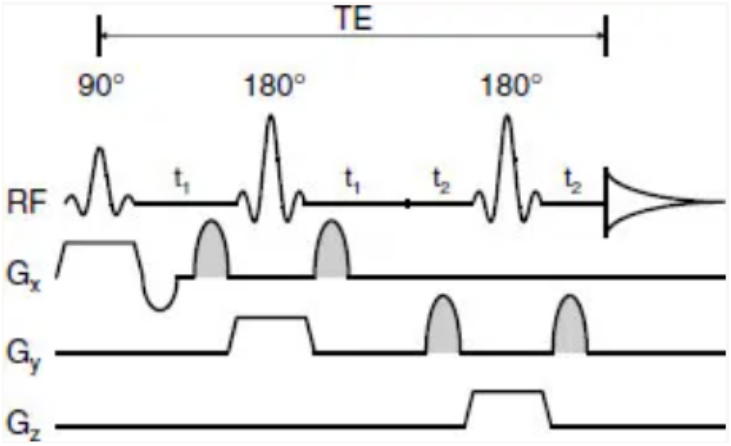

Figure 4.1: Point Resolved Spectroscopy (PRESS) pulse sequence [1]. From top to bottom: the echo time (TE, defined as the interval between the first excitation pulse and the center of signal acquisition), the radiofrequency (RF) pulses, and the magnetic field gradients applied along the x, y, and z axes (G_x, G_y, G_z), all plotted as a function of time

The PRESS [16] localization method is a double spin-echo method, in which slice-selective excitation is combined with two slice-selective refocusing pulses as shown in Figure 4.1. When the first π pulse is executed after a time t_1 following the excitation pulse, a spin-echo is formed at time $2t_1$. The second 180° pulse refocuses this spin-echo during a delay $2t_2$, such that the final spin-echo is formed at time $2t_1 + 2t_2$ (which equals the echo-time of PRESS, i.e. $TE = 2t_1 + 2t_2$). The first echo contains signal from a column which is the intersection between the two orthogonal slices selected by the $\frac{\pi}{2}$ pulse and the first π pulse (selected by the gradients G_x and G_y in Figure 4.1). The second spin-echo only contains signal from the intersection of the three planes selected by the three pulses, resulting in the desired volume (as the third pulse is combined with the application of the gradient G_z). Signal outside the VOI is either not excited or not refocused, leading to rapid dephasing of the signal by the crusher/spoiler magnetic field gradients (as in Figure 4.1, G_x, and G_y are

turned on before and after the π pulses to rapidly de-phase the signal outside the selected voxel) [1].

4.3 In phantom optimization

MRSI slices were acquired on a BRAINO phantom using a 32-channel coil, with FOV dimensions = 180 × 162 mm^2, voxel size = 15 × 15 × 15 mm^3, VOI dimensions = 110 × 100 mm^2, TE = 68 ms, and circular sat bands.
In the acquisitions performed on the BRAINO phantom, all the different parameters described in Section 3.1 were systematically varied: ws methods (excitation, CHESS, MOIST), TR (1000, 1500, 2000, 4000 ms), SENSE (ON/OFF), shimming (Pb_auto vs. PB_volume selection), pulse shape (sharp, normal, classic-long, classic-short), and chemical shift direction (AL, PL, PR, AR).
At the end of this step, the optimized protocol on the phantom was tested across the two different coils to assess the differences between them on the phantom.
To analyze the effect of each parameter variation, 26 different acquisitions were performed, as detailed in Table 4.1.

Acquisition number	Shared parameters	Parameter studied	Set value
1	TR= 1000 ms, SHIM= PB-auto, SENSE= ON, RF pulse set= sharp, Shift dir.= AL	**WS**	excitation
2			MOIST
3			CHESS
4	ws= excitation, SHIM= PB-auto, SENSE= ON, RF pulse set= sharp, Shift dir.= AL	**TR**	1000 ms
5			1500 ms
6			2000 ms
7			4000 ms
8	ws= excitation, TR= 1500 ms, SHIM= PB-auto, RF pulse set= sharp, Shift dir.= AL	**SENSE**	ON
9			OFF
10			ON, NSA= 2
11	ws= excitation, TR= 1500 ms, RF pulse set= sharp, Shift dir.= AL	**Shimming**	Pb_auto, SENSE ON
12			Pb_volume, SENSE ON
13			Pb_auto, SENSE OFF
14			Pb_volume, SENSE OFF
15	ws= excitation, TR= 1500 ms, SHIM= PB-volume, SENSE= OFF, Shift dir.= AL	**RF pulse**	sharp
16			normal
17			classic long
18			classic short
19	ws= excitation, TR= 1500 ms, SHIM= PB-volume, SENSE= OFF, RF pulse set= sharp	**Shift dir**	AL
20			PL
21			AR
22			PR
23	ws= excitation, TR= 1500 ms, SENSE= OFF, RF pulse set= sharp, Shift dir.= AL	**COIL**	multi-channel, SHIM= Pb_auto
24			single-channel, SHIM= Pb_auto
25			multi-channel, SHIM= Pb_volume
26			single-channel, SHIM= Pb_volume

Table 4.1: Details of each of the different 2D PRESS CSI acquisitions on phantom

4.4 In vivo optimization

MRSI slices using the PRESS sequence were acquired in four HCs using a 32-channel coil, with the slice positioned within white matter (WM), as shown in Figure 4.2. The common acquisition parameters were: FOV dimensions = 180 × 162 mm^2, voxel size = 15 × 15 × 15 mm^3, VOI dimensions = 110 × 100 mm^2, TE = 68 ms, and circular sat bands.
In vivo, the effects of shimming (PB-auto vs. PB-volume), SENSE (ON vs. OFF), and WS methods (excitation vs. MOIST) were evaluated again. In addition, the reconstructed voxel size was varied to study the effect of reconstructing voxels smaller than the nominal acquisition size (15 × 15 × 15 mm^3).
Lastly, in anticipation of the coil comparison in the final study, one participant was scanned using both single- and multi-channel coils while varying the shimming method, as done in the final phantom scans.
All scans performed in this second phase of the study are detailed in Table 4.2. Together with these scans for each of the 4 HCs a 3D T1-weighted anatomical image was performed, to allow WM segmentation and correct slice positioning.

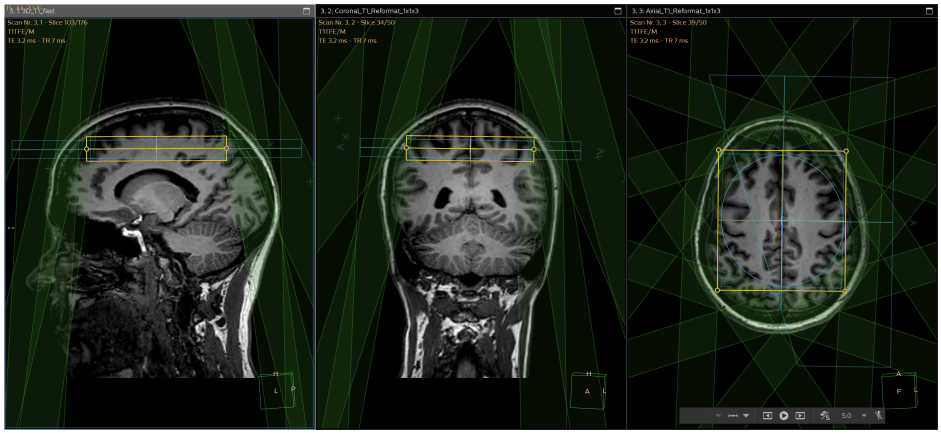

Figure 4.2: 2D CSI slice positioning within white matter in vivo: FOV in blue, shimming volume in yellow, circular sat bands in green.

Acquisition number	Shared parameters	Parameters studied	Set value
1	ws= MOIST, voxel size= 15×15×15 mm^3, TR= 4000 ms, RF pulse set= sharp, Shift dir.= AL	**Shimming and SENSE**	Pb_auto, OFF
2			Pb_auto, ON
3			Pb_auto, ON, NSA=2
4			Pb_volume, ON
5	ws= excitation, TR= 1500 ms, SHIM= PB-auto, SENSE= OFF, RF pulse set= sharp, Shift dir.= AL	**Reconstructed voxel size**	15×15×15 mm^3
6			12×12×15 mm^3,
7			9×9×15 mm^3,
8	voxel size= 15×15×15 mm^3, TR=1500 ms, SHIM=PB-auto, SENSE= OFF, RF pulse set= sharp, Shift dir.= AL	**WS**	excitation
9			MOIST
10	voxel size= 15×15×15 mm^3, ws= MOIST, TR=1500 ms, SENSE= OFF, RF pulse set= sharp, Shift dir.= AL	**COIL**	multi-channel, SHIM= Pb_auto
11			single-channel, SHIM= Pb_auto
12			multi-channel, SHIM= Pb_volume
13			single-channel, SHIM= Pb_volume

Table 4.2: Details of each of the different acquisitions in vivo to optimize scanner parameters

4.5 In vivo coil comparison

To allow for a comparison of coil performance five HCs were scanned using the same acquisition protocol.
Starting with the ^{1}H multi-channel head coil, the acquired scans were:

- Survey
- 3D T1-weighted anatomical image [acquisition time: 7 min]
- 3D T2-weighted FLAIR image [acquisition time: 7 min]
- 2D CSI PRESS acquisition, with the slice positioned as shown in Figure 4.2 [acquisition time: 6 min]

Continuing the protocol with the single-channel coil, the scans performed on all five HCs were:

- Survey
- 3D T1-weighted fast anatomical image [acquisition time: 7 min]
- 2D CSI PRESS acquisition, with the slice positioned as shown in Figure 4.2 [acquisition time: 6 min]

The 2D CSI PRESS acquisitions were performed using common scanner parameters across all five HCs, based on the optimization previously conducted in this study. All PRESS acquisition parameters set in this final part of the study are detailed in the Table 4.3.

PRESS ACQUISITION PARAMETERS	
FOV:	240×182 mm^2
voxel size:	12×12×15 mm^3
VOI:	110×100 mm^2
TE:	68 ms
TR:	1500 ms
sat bands:	circular
ws:	MOIST
SENSE:	OFF
Shimming:	Pb_volume
RF pulse:	sharp
Shift dir:	AL
NSA:	1

Table 4.3: Parameters selection for 2D CSI PRESS acquisition

4.6 Data Analysis

4.6.1 TARQUIN

Preprocessing and fitting of the spectroscopy data was performed using TARQUIN (Totally Automatic Robust Quantitation in NMR) [18]. Following a qualitative assessment of both the TARQUIN and Osprey software packages for spectroscopy analysis, TARQUIN was selected for all processing steps. This choice was driven by its more intuitive graphical user interface (GUI), which enables more precise handling of the fitting process for 2D and potentially 3D

slices. Specifically, TARQUIN displays the spatial distribution maps of metabolites alongside the fitted spectra for each voxel simply by selecting the voxel of interest. In contrast, Osprey is a MATLAB-based tool that does not support GUI-based analysis of 2D acquisitions or voxel-by-voxel spectral display, as it was primarily developed for single-voxel (SV) analysis.
TARQUIN is an open-source software tool used to quantify MRS and MRSI data, allowing for water removal and the fitting of various file formats acquired from MRI scanners (including .SPAR/.SDAT files generated by Philips scanners). The fitting procedure begins with signal preprocessing, consisting of initial point truncation and water suppression. The remaining signal is then modeled in the time domain using a basis set that includes metabolites, lipids, and macromolecules, while a non-negative least-squares projection is used to estimate signal amplitudes. Finally, soft constraints are applied to the least-squares projection to reduce errors associated with over-fitting [18].

Most of the fitting parameters are automatically selected when uploading the .SPAR/.SDAT files to TARQUIN, but specific parameter settings are needed when using TARQUIN to fit phantom data.
The applied indications for BRAINO scans were [19]:
1. The starting PPM reference value was changed from 4,65 to 4,85, due to the strong chemical shift dependence of water on temperature.
2. The PPM reference signal was changed to NAA.
3. The starting point for analysis was reduced to 10 data points, since phantom data do not have significant baseline distortion.
4. The basis set was changed to match the chemicals in the phantom: TARQUIN allows a GE "braino" phantom predefined internal basis to be specified as an option.
5. w_{conc} was changed from a default value of 35880, which assumes a white matter value, to a value of 55556, that is to be used for phantoms [19].
6. w_{att} value was changed according to the formula:

$$w_{\text{att}} = \frac{exp(-t/T_2^{\text{water}})}{exp(-t/T_2^{\text{signal}})} \tag{4.1}$$

Considering that a 3T scanner was used for the measurements, T_2^{water} was set to 60 ms and T_2^{signal} was assumed to be approximately 200 ms (averaged across the T_2 values of the BRAINO metabolites), yielding $w_{\text{att}} = 0,45$. This $w_{\text{att}} = 0.45$ value, as it is related to the use of a 3T scanner was kept the same for the in vivo dataset analysis.

The TARQUIN fitting output is depicted in Figure 4.3. It provides the con-

centration of each metabolite specified in the internal basis set, the associated standard deviation, and the SNR measurement. The concentration of the metabolites is evaluated by TARQUIN in two ways depending on the input files provided: if a water reference file (a reference file with the signal from water that is not suppressed) is provided together with the acquisition file, TARQUIN is able to evaluate an absolute concentration of each metabolite, expressed in mM. If the water reference file is not uploaded, the concentration evaluated by TARQUIN is in arbitrary units, expressed as a ratio with a reference metabolite; the quantity evaluated is therefore relative metabolite ratios.
SNR is evaluated by TARQUIN using the following formula:

$$\mathrm{SNR} = \frac{\text{Maximum in the spectrum} - \text{baseline}}{2 \cdot \text{RMS of the residual between 0,5 and 4 ppm}} \tag{4.2}$$

where the maximum in the spectrum corresponds to the peak height of the NAA signal, and RMS represents the root mean square of the noise, evaluated as the residual between the fit and the spectrum within the 0,5–4,0 ppm range.

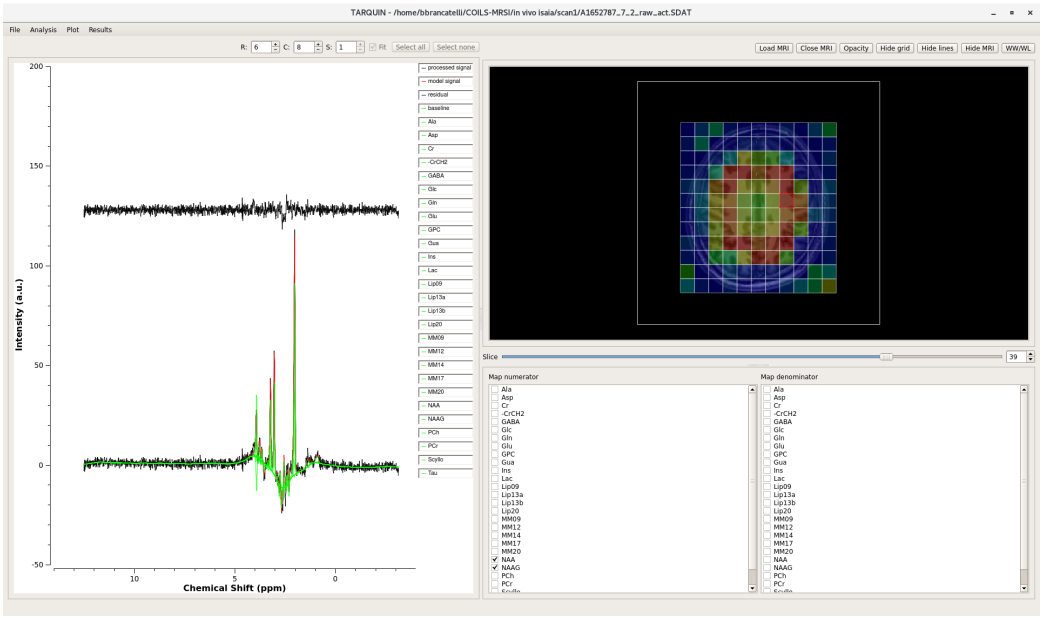

Figure 4.3: TARQUIN fitting performed on a 2D CSI PRESS acquisition taken on a HC. Top left trace: residuals; bottom left: fitted spectrum for a voxel of the CSI grid; top right: NAA map (blu = noise, green = low concentration; yellow = intermediate concentration; red = highest concentration) ; bottom right: list of fitted peaks.

4.6.2 In phantom data analysis

All statistical analyses were performed using a purposly written Python script, developed during this thesis. The TARQUIN output is provided as a .csv file containing a matrix of metabolite concentrations, standard deviations (%SD), and SNR, with one row per voxel. By extracting the voxel-wise SNR and N-acetylaspartate (NAA) concentrations into separate arrays and reshaping them to match the FOV dimensions, spatial heatmaps of SNR and NAA distribution were generated for each acquisition (Figure 4.4a).
The metabolite distribution heatmaps were subsequently masked based on the fit reliability: voxels were considered acceptable only if the %SD was lower than or equal to 20%. Unreliable fits were excluded from the heatmap, yielding the masked maps shown in Figure 4.4b.
This allows 2D visualization of spatial variations in SNR and metabolite quantification.

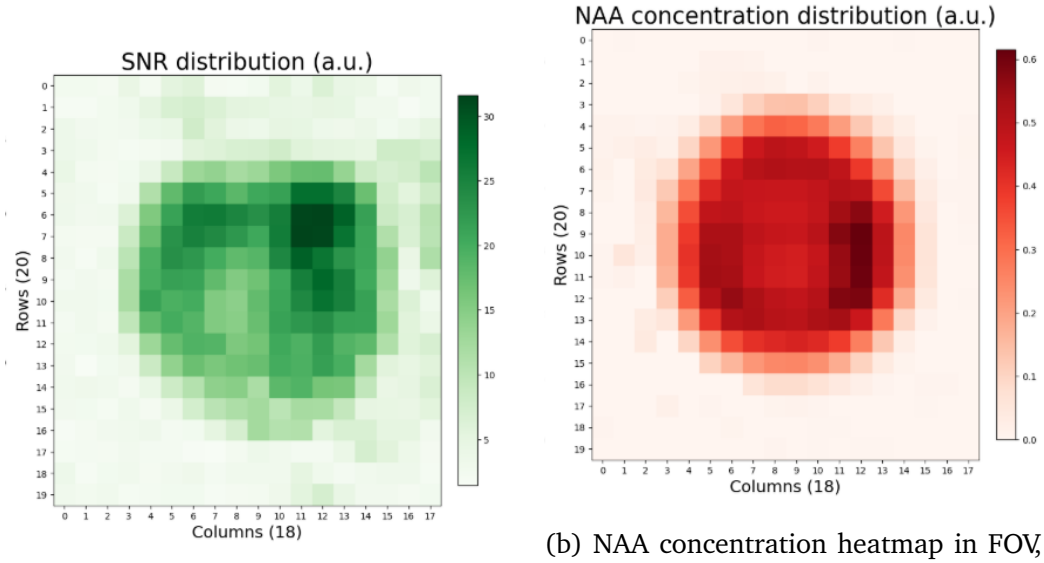

(a) SNR heatmap in FOV

(b) NAA concentration heatmap in FOV, masked with fitting accuracy (%SD<20)

Figure 4.4: Representative distributions of (a) SNR and (b) NAA concentration across the FOV, acquired during phantom optimization.

A similar procedure was applied to the other metabolites quantified by TARQUIN (Figure 4.5); however, NAA was selected as the reference metabolite for further coil and parameter evaluations due to its high concentration across the voxels.

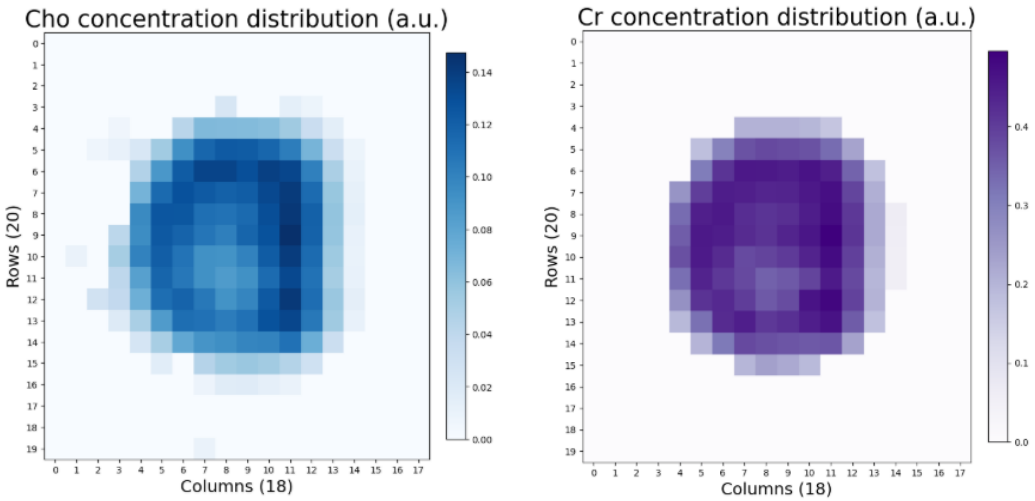

Figure 4.5: Cho and Cr concentration heatmap within the FOV, masked with fitting accuracy (%SD<20)

Since the phantom composition is homogeneous, the spatial distribution of SNR and metabolite concentrations was evaluated. By applying an additional mask to the matrices, only voxels within the VOI (16x12 voxel) were included, and their value distributions were visualized via histograms. Histograms of SNR (Figure 4.6a) and NAA (Figure 4.6b) concentrations were generated for each of the 26 phantom acquisitions.

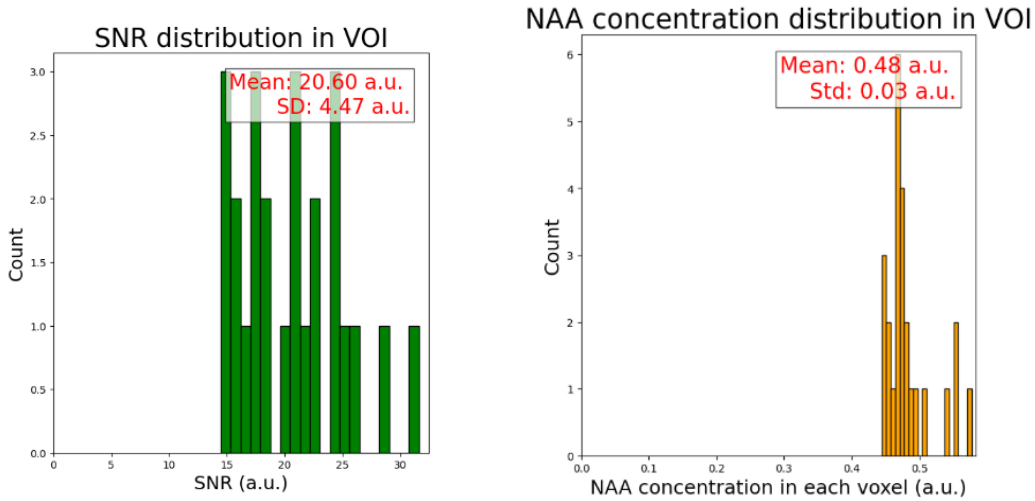

(a) SNR distribution within the VOI (b) NAA distribution within the VOI

Figure 4.6: Histograms showing (a) SNR and (b) NAA concentration distributions within the VOI, acquired during phantom optimization.

To compare the acquisitions, the mean and SD of each distribution were calculated, and normality was formally assessed, with Shapiro-Wilk tests and Quantile-Quantile Plot performed for each acquisition (Figure 4.7).

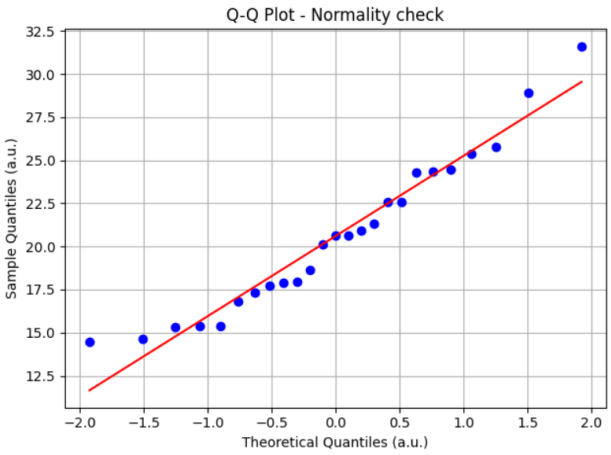

Figure 4.7: Quantile-Quantile plot evaluating the normality of an SNR distribution. Each blue dot is a voxel of the VOI

Boxplots were generated to compare SNR and NAA concentration distributions across related acquisitions, grouped according to Table 4.1 (grouped acquisitions corresponded to a set of experiments where only a single parameter was varied).
To assess whether statistically significant differences existed between acquisitions, a one-way ANOVA was performed if distributions met normality assumptions; otherwise, the non-parametric Kruskal-Wallis test was used. The Mann-Whitney U test was performed to compare pairs of acquisitions.
In the presence of a statistically significant difference ($p < 0,05$), the acquisition yielding the highest mean SNR was identified as the optimal parameter setting for the parameter varied in that group.

4.6.3 In vivo data analysis

For the in vivo data analysis, the same procedure used for the in phantom SNR data was followed: after extracting the voxel-by-voxel SNR from the TARQUIN fitting, spatial heatmaps were created (as in Figure 4.4a) along with histograms and boxplots showing the SNR distribution within the VOI. To compare the SNR results, data normality was assessed, followed by ANOVA or the non-parametric Kruskal–Wallis test to evaluate statistical significance. In the

final part of the study, the SNR distribution for each subject was analysed by comparing the results obtained with the 32-channel and the single-channel head coil.

To evaluate the distribution of metabolite concentrations, performed in the final part of this study, the analysis required several preliminary steps: the white matter (WM) and gray matter (GM) volume fractions in each voxel were extracted from the 3D-T1 weighted images acquired for each subject. This allowed for linear regression between the WM fraction and NAA concentration to estimate metabolite levels in pure WM voxels. This step was not needed in the previous analysis because the CSI grid from grouped protocols were positioned in the same way, hence the voxels were assumed to be of identical tissue composition.

Brain segmentation

Brain segmentation was performed using the 3D-T1 weighted images acquired for each HC and with each coil configuration. DICOM images were first converted to NIfTI format using the `dcm2nii` tool [20]. Automated tissue segmentation and anatomical parcellation were subsequently performed on the resulting NIfTI files using the Geodesic Information Flows (GIF) framework [21]. This pipeline allowed the extraction of tissue probability maps for GM, WM, and cerebrospinal fluid (CSF). Representative results of this segmentation are shown in Figure 4.8.
Following tissue segmentation, the 4D probabilistic tissue maps obtained from GIF were converted into a 3D discrete label map (hard segmentation) using the `seg_maths` utility (`-tpmax` operation) from the NiftySeg package [22]. This operation assigns each voxel a discrete integer label corresponding to the tissue class with the highest posterior probability. In this way, each voxel was unambiguously assigned to a single tissue class, with intensity values defined as 1 for CSF, 2 for GM, 3 for WM and 0 for non-brain background.

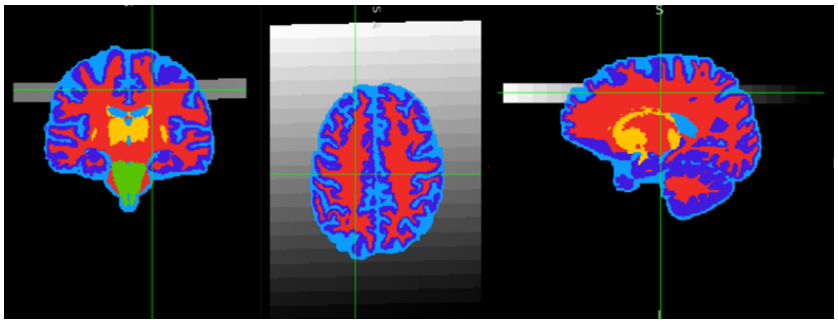

Figure 4.8: Brain segmentation results: data are extracted form a 3D-T1 image on a HC, shown in the same space of the MRSI grid (in gray). WM is shown in red, GM in blue and CSF in light blue

WM percentage calculation

To evaluate tissue volume fractions within each spectroscopic voxel, the low-resolution MRSI grid had to be spatially aligned with the high-resolution anatomical segmentation map. The MRS acquisition geometry stored in the Philips `.spar` header was first converted into NIfTI format using an in-house Python script (`spar2nifti.py`), generating a labeled MRS mask where each voxel position is identified by a unique integer index. The resulting mask was subsequently coregistered and resampled onto the high-resolution T1 segmentation space using `reg_resample` from the NiftyReg package [23]. Nearest-neighbor interpolation (`-inter 0`) was employed to prevent label blurring and preserve discrete voxel boundaries.
Bringing the spectroscopic grid and the 3D anatomical segmentation into the same reference space enabled the precise calculation of voxel-wise tissue fractions (GM, WM, and CSF) within the MRS volume of interest. By loading both the MRSI grid mask and the tissue segmentation into Python, each anatomical voxel in the coregistered volume was uniquely characterized by its discrete tissue class and the index of the resampled MRSI voxel it fell within. For each spectroscopic voxel index (ranging from 1 to 336), a spatial mask was applied to isolate the intersecting anatomical voxels. The relative percentage of each tissue compartment was then determined by calculating the proportion of voxels carrying each tissue label relative to the total number of anatomical voxels within that spectroscopic mask. Finally, the resulting tissue fractions for each MRSI grid voxel were exported to a `.csv` file for downstream analysis. The resulting WM distribution in the MRSI grid is shown in Figure 4.9.

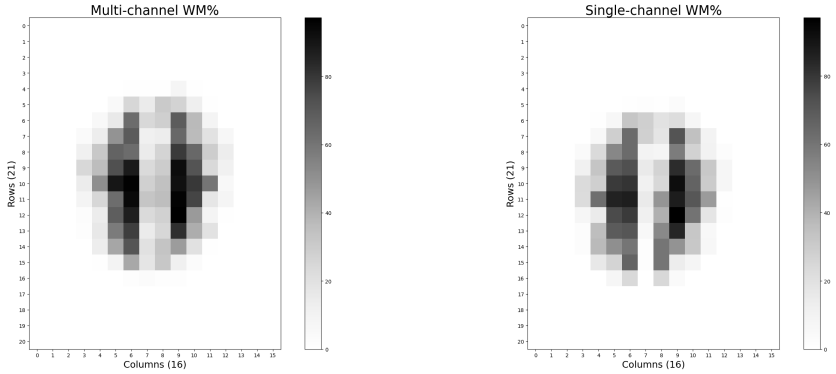

Figure 4.9: Heatmap showing the WM percentage in the MRSI grid, extracted form the multi-channel measurements on the left and form the single-channel ones on the right.

NAA concentration analysis

The total NAA concentration within each MRSI voxel, as quantified by TARQUIN, represents the combined in vivo contribution of both WM and GM, expressed as:

$$C_{\mathrm{T}} = f_{\mathrm{WM}} \cdot C_{\mathrm{WM}} + f_{\mathrm{GM}} \cdot C_{\mathrm{GM}} \tag{4.3}$$

where C_{T} is the total NAA concentration estimated from the spectral fitting, f_{WM} and f_{GM} denote the respective voxel volume fractions of WM and GM determined in the previous section, and C_{WM} and C_{GM} represent the pure tissue concentrations of NAA in WM and GM, respectively.
By defining the total fraction as $f_{\mathrm{T}} = f_{\mathrm{WM}} + f_{\mathrm{GM}}$, Equation 4.3 can be normalized as:

$$\frac{C_{\mathrm{T}}}{f_{\mathrm{T}}} = \frac{f_{\mathrm{WM}}}{f_{\mathrm{T}}} \cdot C_{\mathrm{WM}} + \left(1 - \frac{f_{\mathrm{WM}}}{f_{\mathrm{T}}}\right) \cdot C_{\mathrm{GM}} \tag{4.4}$$

This formulation enables the estimation of pure tissue concentrations through linear regression (Figure 4.10a), with $x = \frac{f_{\mathrm{WM}}}{f_{\mathrm{T}}}$ and $y = \frac{C_{\mathrm{T}}}{f_{\mathrm{T}}}$:

$$y = (C_{\mathrm{WM}} - C_{\mathrm{GM}}) \cdot x + C_{\mathrm{GM}} \tag{4.5}$$

This relationship was assessed for each subject using simple ordinary least squares (OLS) linear regression:

$$y = \beta_0 + \beta_1 \cdot x + \varepsilon$$

Model goodness-of-fit was evaluated using the coefficient of determination (R^2), reflecting the proportion of variance in the dependent variable accounted for by the linear fit. To evaluate the statistical significance of the linear fit, a

two-tailed Student's t-test on the regression model was performed, rejecting the null hypothesis (i.e., that the observed relationship occurred by chance) at $p < 0,05$. In addition, the regression residuals were visually assessed, as shown in the plot in Figure 4.10b.

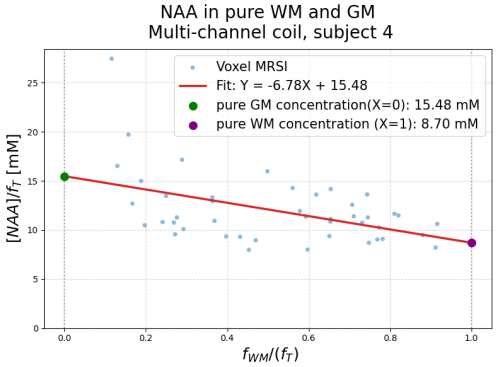

(a) Linear fit to estimate NAA concentration in WM

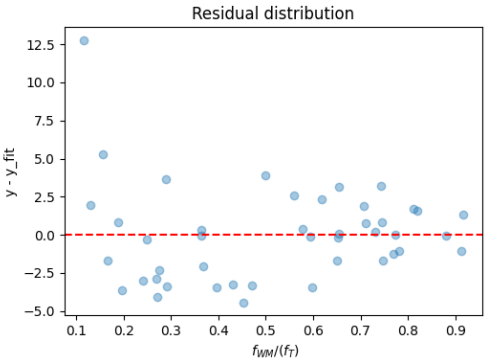

(b) Fit residual distribution

Figure 4.10: (a) Linear fit of NAA concentration as a function of white matter fraction in each voxel, to estimate concentration in pure WM, and (b) the associated residual distribution, evaluated in one of the five HCs scanned for the coil comparison.

To determine whether the linear regressions obtained from the single-channel and multi-channel coils were statistically distinguishable, a multiple OLS linear regression model with an interaction term was implemented. Differences between the two fits were evaluated based on the estimated regression coefficients (β) and their associated two-tailed p-values derived from Student's t-tests: the interaction parameter (β_{int}) assessed whether the slopes of the two regression lines differed significantly while the main coil effect (β_{coil}) evaluated potential baseline differences in the intercept. All statistical hypotheses were tested at a significance threshold of $0,05$.

Chapter 5

Results

5.1 In phantom optimization

In this section, the results of the phantom parameter optimization are presented, divided into subsections according to the evaluated parameter.
For each evaluated parameter, two boxplots are shown grouped in Figure 5.3 and in Figure 5.4, illustrating the variations in the distributions of SNR and NAA concentrations. Each bar refers to a single acquisition, with the investigated parameter specified on the x-axis, representing the SNR or NAA concentration values across all voxels within the VOI, grouped into a single distribution.
Alongside the boxplots, two or three tables are provided: the first table reports the acquisition time for each scan, along with the mean and SD of the SNR across all voxels in the VOI. To determine whether varying the acquisition parameter yields statistically significant differences, normality test outcomes (Y = yes, N = no) and corresponding p-values are reported, evaluated either across all three or four scans or between specific pairwise acquisitions. The second table in each section follows the same structure, reporting the mean and SD of NAA concentration in arbitrary units (a.u.). The decision to analyze metabolite concentrations in a.u. rather than mM was made based on the metabolite distribution heatmaps: likely due to water suppression methods or saturation bands, the concentration distribution in mM appeared noticeably less homogeneous than expected in the phantom, as shown in Figure 5.1. Metabolite concentrations in mM are included in a third table only when relevant for further considerations regarding the parameter, or for the final four phantom acquisitions. The latter were acquired using different coils; in that case, concentrations in a.u. were unsuitable for statistical analysis due to differing scales in relative metabolite ratios.

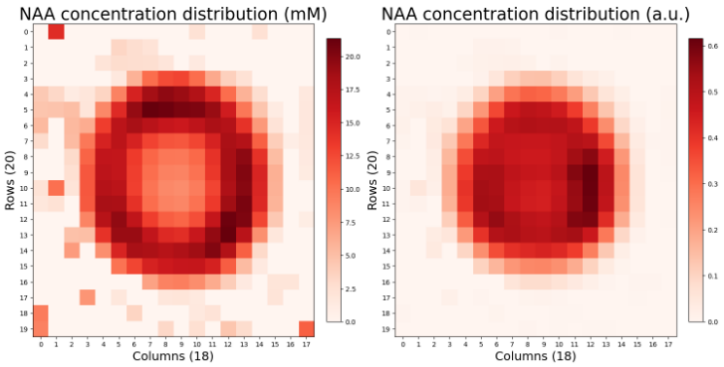

Figure 5.1: Difference in results homogeneity between NAA concentration distribution first evaluated in mM and then in a.u., as relative metabolite ratio.

WS

Scan #	WS	Acq. time	Average SNR (a.u.)	SD (a.u.)	Normality check	p-value
1	excitation	55 s	15,5	4,4	Y	<0,05
2	MOIST	55 s	12,5	4,1	N	
3	CHESS	55 s	11,8	4,8	N	

Table 5.1: Scanning time and average SNR varying WS parameter.

Scan #	WS	Average NAA (a.u.)	SD (a.u.)	Normality check	p-value
1	excitation	0,42	0,03	Y	<0,05
2	MOIST	0,50	0,04	N	
3	CHESS	0,57	0,07	N	

Table 5.2: Average NAA concentration estimated varying WS parameter

TR

Scan #	TR (ms)	Acq. time	Average SNR (a.u.)	SD (a.u.)	Normality check	p-value
4	1000	55 s	15,5	4,4	Y	<0,05
5	1500	1,22 min	21,1	4,8	N	
6	2000	1,50 min	17,7	5,3	N	
7	4000	3,40 min	18,4	4,2	Y	

Table 5.3: Scanning time and average SNR varying TR.

Scan #	TR (ms)	Average NAA (a.u.)	SD (a.u.)	Normality check	p-value
4	1000	0,42	0,03	Y	<0,05
5	1500	0,60	0,03	Y	
6	2000	0,68	0,04	N	
7	4000	0,63	0,04	Y	

Table 5.4: Average NAA concentration estimated varying TR

SENSE

Scan #	SENSE	Acq. time	Average SNR (a.u.)	SD (a.u.)	Normality check	p-value
8	ON	1,22 min	14,6	4,9	N	0,068
9	OFF	2,43 min	17,8	5,0	Y	
10	ON, NSA=2	2,37 min	16,2	4,7	Y	

Table 5.5: Scanning time and average SNR varying SENSE parameter.

Scan #	SENSE	Average NAA (a.u.)	SD (a.u.)	Normality check	p-value
8	ON	0,47	0,04	Y	0,24
9	OFF	0,49	0,04	N	
10	ON, NSA=2	0,48	0,05	N	

Table 5.6: Average NAA concentration in a.u. estimated varying SENSE parameter.

Scan #	SENSE	Average NAA (mM)	SD (mM)	Normality check	p-value
8	ON	7,4	1,7	Y	<0,05
9	OFF	10,9	2,0	N	
10	ON, NSA=2	7,6	1,7	Y	

Table 5.7: Average NAA concentration in mM estimated varying SENSE parameter.

SHIMMING

Scan #	SHIMM	Acq. time	Average SNR (a.u.)	SD (a.u.)	Normality check	p-value	p-value
11	Pb_auto SENSE ON	1,22 min	14,6	4,9	N	<0,05	0,15
12	Pb_volume SENSE ON	1,22 min	15,9	4,1	Y		
13	Pb_auto SENSE OFF	2,43 min	17,8	5,0	Y		<0,05
14	Pb_volume SENSE OFF	2,43 min	20,6	4,5	Y		

Table 5.8: Scanning time and average SNR varying SHIMMING parameter.

A statistically significant difference in SNR distributions was observed between SENSE ON and OFF for both shimming methods (scan 11 vs. scan 13, shim = Pb_auto, $p < 0,05$; scan 12 vs. scan 14, shim = Pb_volume, $p < 0,05$).The largest increase in SNR in the phantom parameter optimization study was achieved by setting shimming to Pb_volume and SENSE to OFF, yielding an average SNR of 20,6 compared to 14,6 with Pb_auto and SENSE ON.

Scan #	SHIMM	Average NAA (a.u.)	SD (a.u.)	Normality check	p-value	p-value
11	Pb_auto SENSE ON	0,47	0,04	Y	<0,05	<0,05
12	Pb_volume SENSE ON	0,51	0,05	N		
13	Pb_auto SENSE OFF	0,49	0,04	N		0,28
14	Pb_volume SENSE OFF	0,48	0,03	N		

Table 5.9: Average NAA concentration in a.u. estimated varying SHIMMING parameter.

Scan #	SHIMM	Average NAA (mM)	SD (mM)	Normality check	p-value	p-value
11	Pb_auto SENSE ON	7,4	1,7	Y	<0,05	0,17
12	Pb_volume SENSE ON	8,0	1,7	N		
13	Pb_auto SENSE OFF	10,9	2,1	N		0,92
14	Pb_volume SENSE OFF	10,9	1,9	Y		

Table 5.10: Average NAA concentration in mM estimated varying SHIMMING parameter.

NAA concentration (mM) distributions was observed as statistically different between SENSE ON and OFF for both shimming methods (scan 11 vs. scan 13, shim = Pb_auto, $p < 0,05$; scan 12 vs. scan 14, shim = Pb_volume, $p < 0,05$).

RF pulse

Scan #	RF pulse	Acq. time	Average SNR (a.u.)	SD (a.u.)	Normality check	p-value
15	sharp	2,43 min	16,8	5,2	Y	<0,05
16	normal	2,43 min	14,8	4,7	N	
17	classic long	2,43 min	18,9	3,1	N	
18	classic short	2,43 min	17,7	3,3	Y	

Table 5.11: Scanning time and average SNR varying RF pulse shape.

Scan #	RF pulse	Average NAA (a.u.)	SD (a.u.)	Normality check	p-value
15	sharp	0,50	0,04	Y	<0,05
16	normal	0,45	0,03	Y	
17	classic long	0,45	0,02	Y	
18	classic short	0,34	0,02	Y	

Table 5.12: Average NAA concentration estimated varying RF pulse shape.

Chemical shift dir.

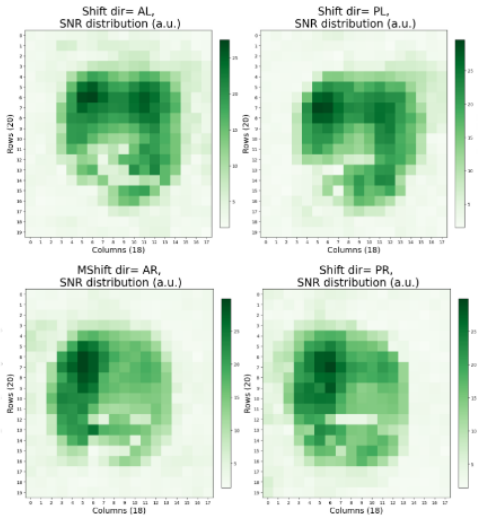

Figure 5.2: Distribution of the SNR varying the Chemical Shift direction.

Single-channel vs Multi-channel coil

Scan #	**COIL SHIMMING**	**Acq. time**	**Average SNR (a.u.)**	**SD (a.u.)**	**Normality check**	**p-value**	**p-value**
23	Multi-channel Pb_auto	2,43 min	17,8	5,0	Y	<0,05	<0,05
24	Single-channel Pb_auto	2,43 min	9,4	2,1	Y		
25	Multi-channel Pb_volume	2,43 min	20,6	4,5	Y		<0,05
26	Single-channel Pb_volume	2,43 min	17,1	3,2	Y		

Table 5.13: Scanning time and average SNR changing coils and varying Shimming parameter.

Scan #	**SENSE**	**Average NAA (mM)**	**SD (mM)**	**Normality check**	**p-value**	**p-value**
23	Multi-channel Pb_auto	10,9	2,1	N	<0,05	<0,05
24	Single-channel Pb_auto	9,2	0,8	Y		
25	Multi-channel Pb_volume	10,9	1,9	Y		0,28
26	Single-channel Pb_volume	9,5	1,0	Y		

Table 5.14: Average NAA concentration in mM estimated changing coil and varying SHIMMING parameter.

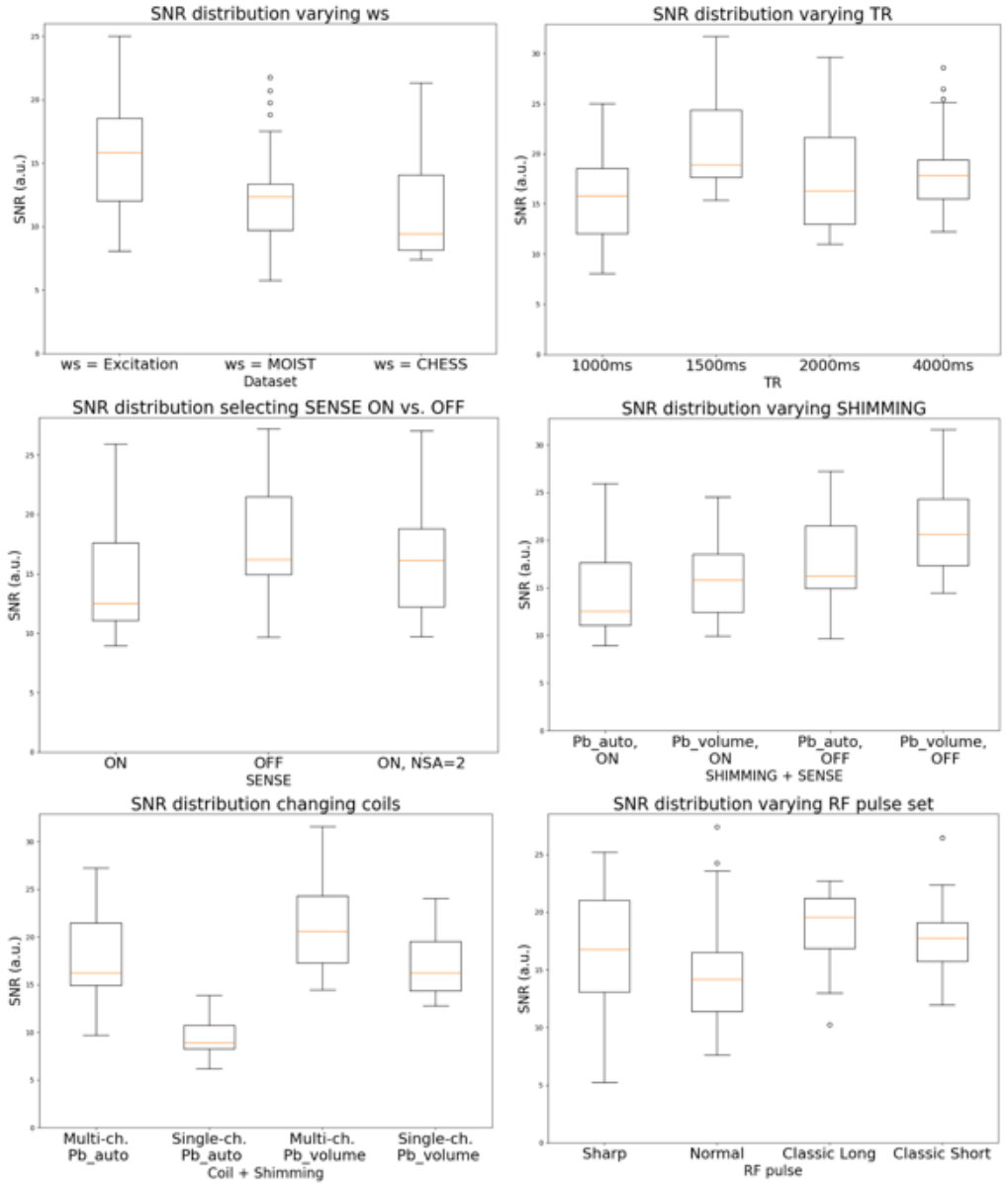

Figure 5.3: SNR distribution resulting form the acquisition in the phantom, grouped in boxplots depending on the varied parameter.

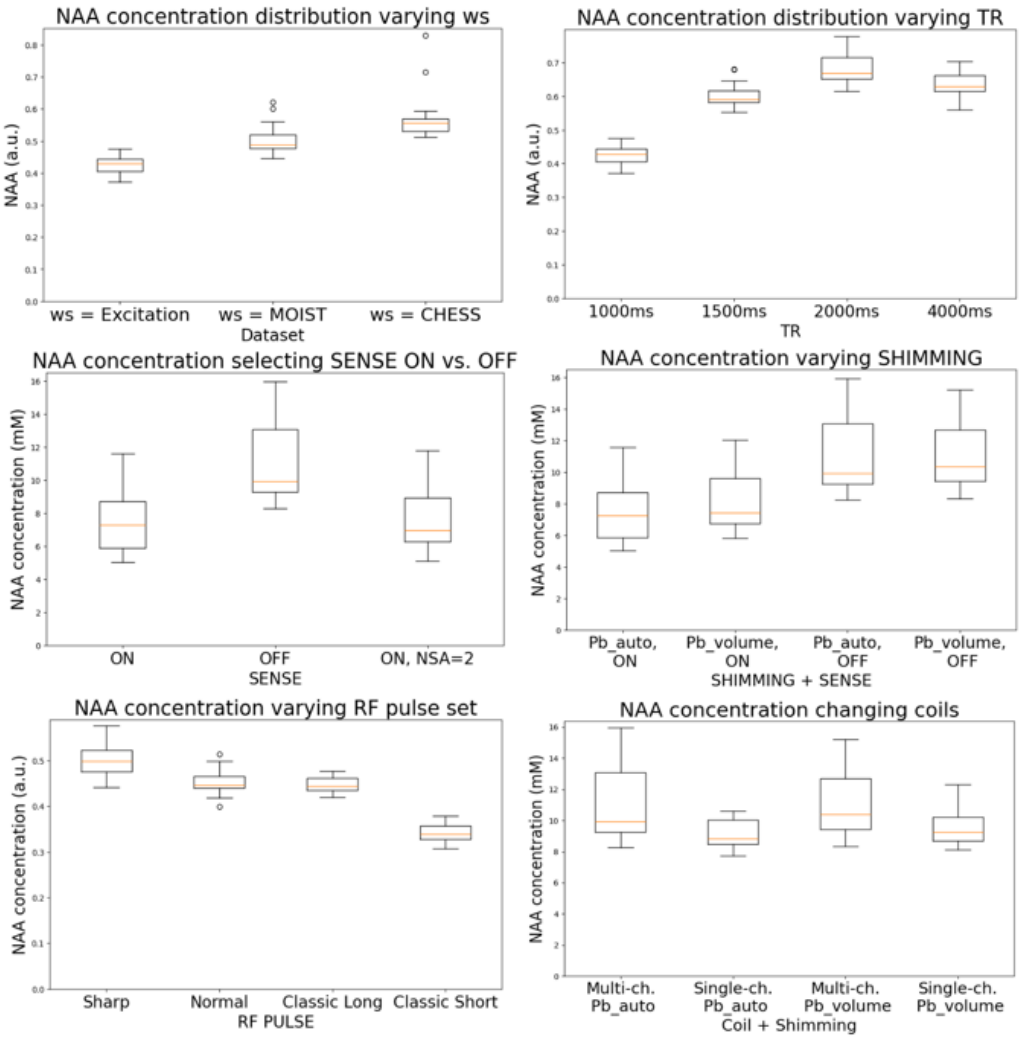

Figure 5.4: NAA distribution resulting form the acquisition in phantom, grouped in boxplots depending on the varied parameter.

5.2 In vivo parameter optimization

This section presents the in vivo parameter optimization results, structured according to the parameters varied within each subject across a total of four subjects (and thus divided into four subsections). In the first subject, the effects of enabling/disabling SENSE and using automatic versus manual volume selection for shimming were evaluated. In the second and third subjects, the reconstructed voxel size and the water suppression method were varied, respectively. In the fourth subject, a preliminary coil comparison was conducted,

evaluating the impact of the shimming method for both coils. For each acquisition, the mean SNR and SD within the VOI are reported, along with the normality assessment of the SNR distributions and the p-values used to evaluate statistically significant differences. Finally, all SNR distributions are displayed as boxplots in Figure 5.5, where each dataset represents an acquisition SNR distribution and scans acquired on the same subject are directly compared.

Shimming and SENSE

Scan #	**SHIMM, Acceleration**	**Acq. time**	**Average SNR (a.u.)**	**SD (a.u.)**	**Normality check**	**p-value**
1	Pb_auto, SENSE OFF	7:16 min	26,8	5,7	N	<0,05
2	Pb_auto, SENSE ON	3:40 min	22,6	4,7	N	
3	Pb_auto, SENSE ON NSA=2	7:00 min	26,6	5,4	N	
4	Pb_volume, SENSE ON	3:40 min	25,1	2,9	N	

Table 5.15: Scanning time and average SNR varying SHIMMING and SENSE parameters in vivo.

Acquisition 1, 2, and 3, which were taken by selecting an automatic shimming volume and varying the SENSE parameter (OFF, ON, ON NSA=2), have SNR distributions that are statistically different ($p<0,05$).
Acquisitions 1 and 4, which had SENSE ON while varying the shimming (automatic or manual volume selection), also have SNR distributions that are statistically different ($p<0,05$).
The first three acquisitions were performed with shimming set to Pb_auto, comparing SENSE ON, SENSE OFF, and SENSE ON with NSA $= 2$. In vivo, disabling acceleration doubled the scan time from 3:40 min to 7:14 min. This time increase was deemed clinically acceptable (< 10 min) and was justified by a statistically significant improvement in mean SNR, which increased from 22,6 a.u. to 26,8 a.u. Setting NSA $= 2$ with SENSE ON resulted in comparable mean SNR (26,6 a.u.) and acquisition time (7:00 min) to the fully sampled (SENSE OFF) scan.

Reconstructed voxel size

Scan #	recon. voxel size	Acq. time	Average SNR (a.u.)	SD (a.u.)	Normality check	p-value
5	15x15x15 mm^3	2:43 min	23,9	4,6	N	<0,05
6	12x12x15 mm^3	4:17 min	22,1	5,4	Y	
7	9x9x15 mm^3	7:52 min	19,6	4,9	N	

Table 5.16: Scanning time and average SNR varying reconstructed voxel size in vivo.

Reconstructing voxels to the nominal acquisition dimensions (15×15×15 mm^3) required an acquisition time of 2:43 min and yielded an SNR $= 23,9$ a.u.; reducing the dimensions to $12 \times 12 \times 15$ mm^3 and $9 \times 9 \times 15$ mm^3 extended the acquisition times to 4:17 min and 7:52 min, while reducing the SNR to 22,1 a.u. and 19,6 a.u., respectively. These results demonstrates that higher spatial resolution is feasible at the expense of longer scan times while maintaining acceptable SNR levels.

WS

Scan #	WS	Acq. time	Average SNR (a.u.)	SD (a.u.)	Normality check	p-value
8	excitation	2:43 min	23,9	4,6	N	0,43
9	MOIST	2:43 min	22,4	6,12	N	

Table 5.17: Scanning time and average SNR varying WS parameter in vivo.

Single-channel vs Multi-channel coil

Scan #	**COIL SHIMMING**	**Acq. time**	**Average SNR (a.u.)**	**SD (a.u.)**	**Normality check**	**p-value**	**p-value**
10	Multi-channel Pb_auto	2:43 min	23,0	5,5	N	<0,05	<0,05
11	Single-channel Pb_auto	2:43 min	12,3	3,8	N		
12	Multi-channel Pb_volume	2:43 min	20,4	5,8	N		<0,05
13	Single-channel Pb_volume	2:43 min	13,5	4,5	N		

Table 5.18: Scanning time and average SNR changing coils and varying Shimming parameter in vivo.

Acquisitions 10 and 12, which were taken with the multi-channel coil by selecting automatic vs manual shimming volumes have SNR distributions that are statistically different ($p<0,05$).
Acquisitions 11 and 13, which were taken with the single-channel coil by selecting automatic vs manual shimming volumes also have SNR distributions that are statistically different ($p<0,05$). In agreement with the phantom results, the multi-channel coil yielded a statistically significant improvement in average SNR in vivo (SNR multi/single-channel = 23,0/12,3 a.u. with Pb_auto, and 20,4/13,5 a.u. with Pb_volume).

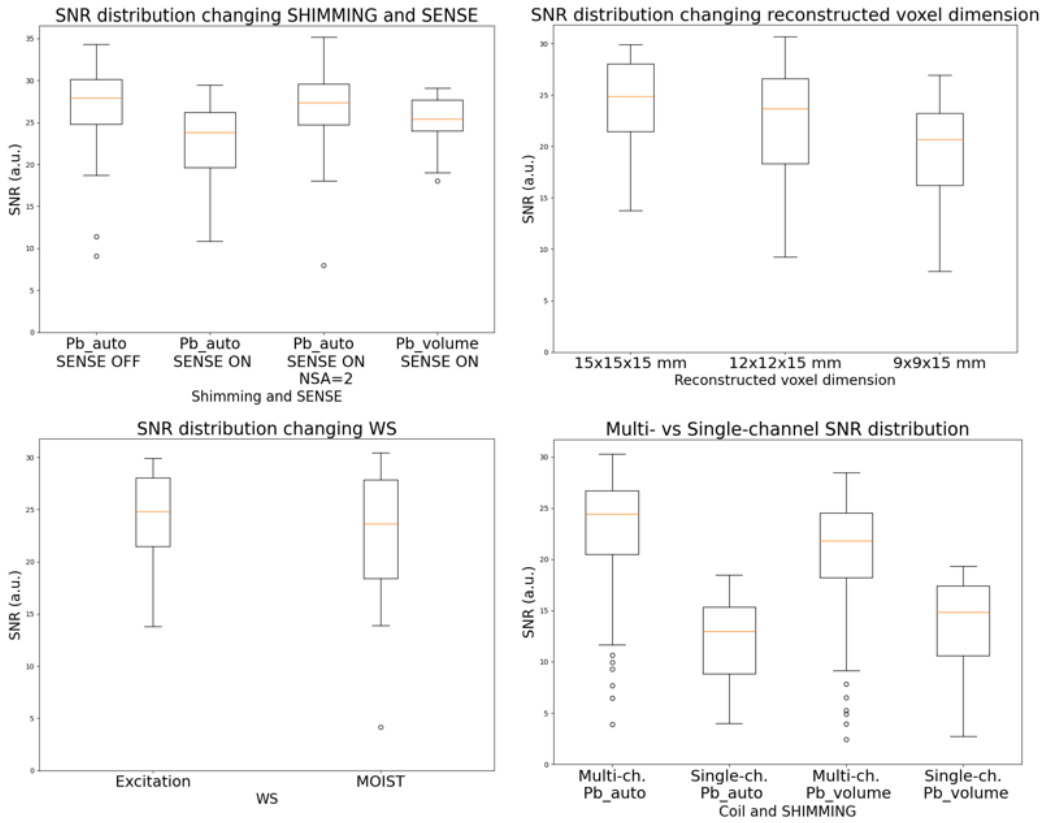

Figure 5.5: SNR distribution resulting form the acquisition of phantom data, grouped in boxplots depending on the varied parameter.

5.3 In vivo coil comparison

This section presents the results obtained from five HCs scanned using the same protocol across both coils, aiming to assess whether one coil outperforms the other in MRSI acquisition. For each subject, two SNR distributions within the VOI were evaluated to characterize the acquisitions from the respective coils. Following WM and GM segmentation for each scan (5 subjects $\times$ 2 coils), a linear regression of the NAA concentration was performed to estimate pure WM NAA values. These values are compared to evaluate potential differences between the two coils in metabolite quantification.

5.3.1 SNR results

	average SNR ± SD (a.u.) Multi-channel coil	average SNR ± SD (a.u.) Single-channel coil	p-value
Subject 1	25,2 ± 2,4	13,7 ± 2,6	<0,05
Subject 2	25,3 ± 3,5	11,5 ± 2,0	<0,05
Subject 3	25,2 ± 3,7	9,8 ± 1,7	<0,05
Subject 4	24,2 ± 4,7	7,4 ± 1,5	<0,05
Subject 5	27,6 ± 3,9	13,4 ± 1,5	<0,05

Table 5.19: SNR results in VOI evaluated scanning 5 Hc with multi-channel and single-channel coil

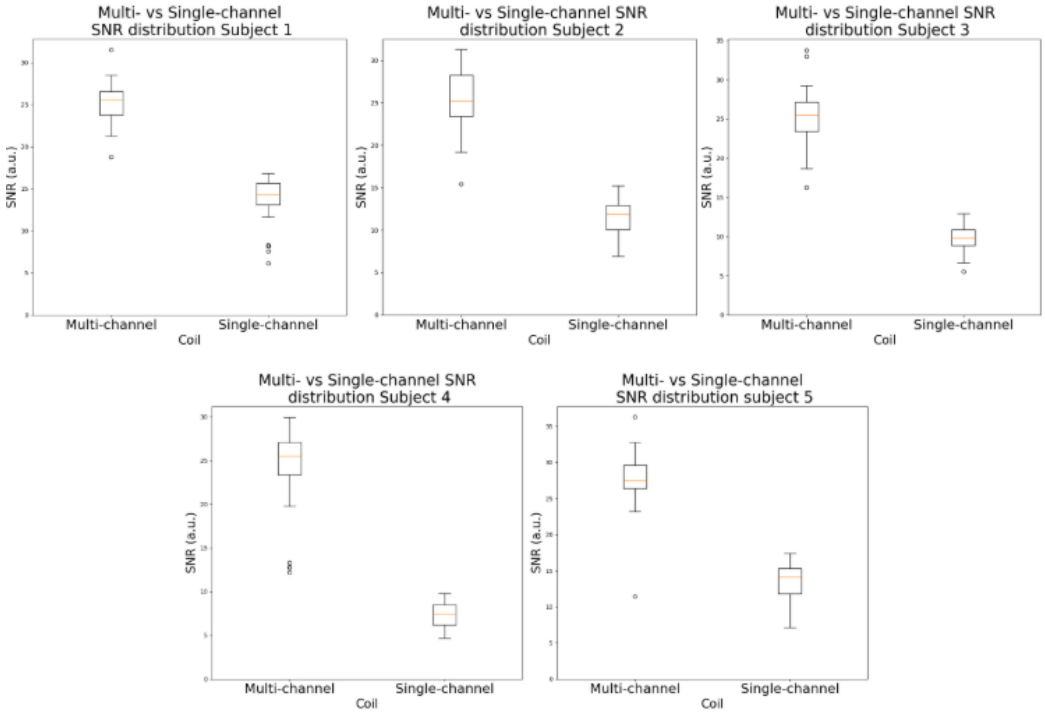

Figure 5.6: Boxplots showing SNR in vivo distribution, comparing for each subject the multi-channel with the single-channel acquisition.

Across all subjects, the mean VOI SNR achieved with the multi-channel head coil was $25,5 \pm 1,2$ a.u., whereas the single-channel coil yielded $11,2 \pm 2,6$ a.u., representing a 128% increase (or a $2,28\times$ factor) in average SNR over the single-channel coil.

5.3.2 NAA concentration results

The regression parameters and estimated pure WM NAA concentrations for the five subjects scanned with the multi-channel coil are reported in Table 5.20, while Table 5.21 summarizes the corresponding results obtained using the single-channel coil. The linear model reached statistical significance (rejecting the null hypothesis, $p < 0,05$) for all participants except Subject 5.
The number of fitted voxels in the single-channel acquisition was substantially lower than in the multi-channel acquisition, ranging from only 13 to 19 out of 49 total voxels in the VOI (indicating that over half of the spectra were rejected, as depicted in the NAA concentration heatmaps in Figure 5.7). Conversely, linear fitting on the multi-channel acquisition incorporated between 43 and 49 voxels per VOI, demonstrating that TARQUIN successfully fitted the NAA resonance in the vast majority of voxels under the quality criterion (SD% < 20).

	NAA conc. in WM (mM) Multi-channel coil	voxel fitted	R^2	p-value fitting	confidence interval
Subject 1	13,6 ± 1,1	48	0,099	<0,05	[11,3; 15,9]
Subject 2	10,4 ± 1,2	43	0,20	<0,05	[8,0; 12,9]
Subject 3	12,0 ± 1,3	49	0,097	<0,05	[9,4; 14,7]
Subject 4	8,7 ± 1,0	44	0,21	<0,05	[6,5; 10,9]
Subject 5	12,7 ± 1,4	47	0,055	0,11	[9,8; 15,5]

Table 5.20: NAA quantification in WM evaluated via linear regression across five HCs scanned with both multi-channel and single-channel coils. Along with NAA concentrations, the p-values of the fit and the number of voxels successfully quantified by TARQUIN are reported.

	NAA conc. in WM (mM) Single-channel coil	voxel fitted	R^2	p-value fitting	confidence interval
Subject 1	7,7 ± 1,4	19	0,36	<0,05	[4,7; 10,8]
Subject 2	7,7 ± 1,7	14	0,43	<0,05	[3,9; 11,4]
Subject 3	7,3 ± 1,3	13	0,42	<0,05	[4,5 ; 10,1]
Subject 5	8,21 ± 1,4	15	0,22	0,07	[5,1 ; 11,3]

Table 5.21: NAA quantification in WM evaluated via linear regression across five HCs scanned with both multi-channel and single-channel coils. Along with NAA concentrations, the p-values of the fit and the number of voxels successfully quantified by TARQUIN are reported.

	β_{coil}	p-value$_{coil}$	β_{int}	p-value$_{int}$
Subject 1	-5,80	<0,05	-3,1	0,43
Subject 2	-2,76	0,17	-2,18	0,56
Subject 3	-4,70	0,07	-1,56	0,76
Subject 5	-4,47	0,08	-0,19	0,85

Table 5.22: multiple OLS linear regression results, comparing multi-channel and single-channel coil for each subject. β_{coil} evaluate differences in the intercept, while β_{int} evaluate differences in slopes of the two regression.

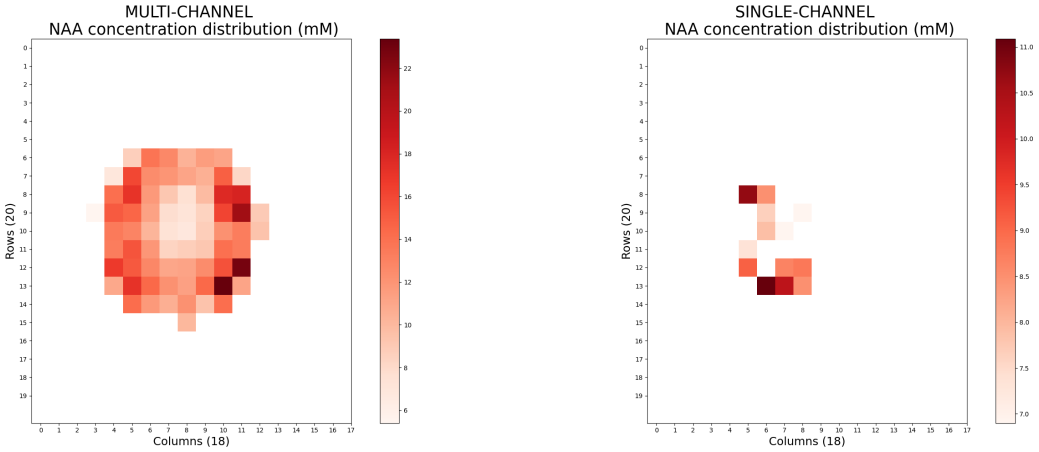

Figure 5.7: NAA concentration heatmaps, evaluated on the same subject with the multi-channel (on the left) and single-channel coil (on the right). Values have been masked with fitting accuracy (%SD<20)

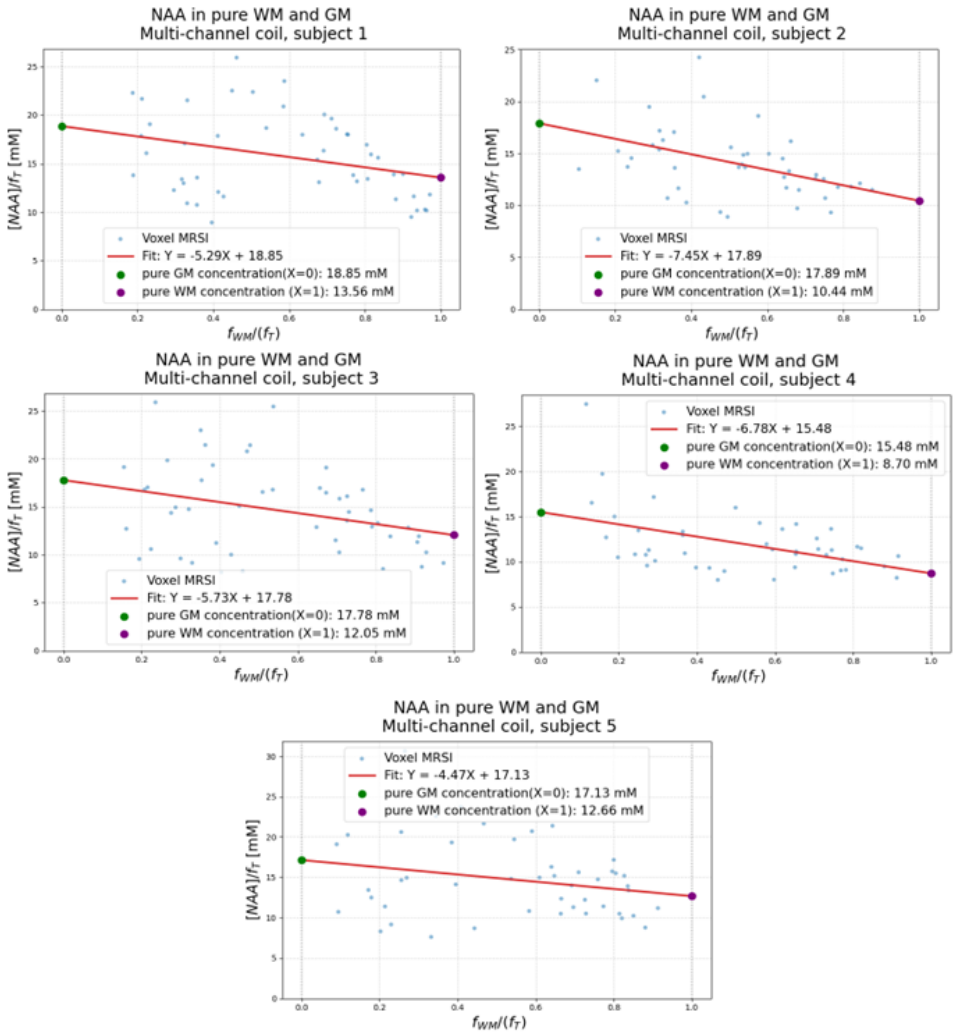

Figure 5.8: Linear fitting of C_T/f_T as function of f_{WM}/f_T following the Equation 4.5. Data are acquired for every subject with the multi-channel coil.

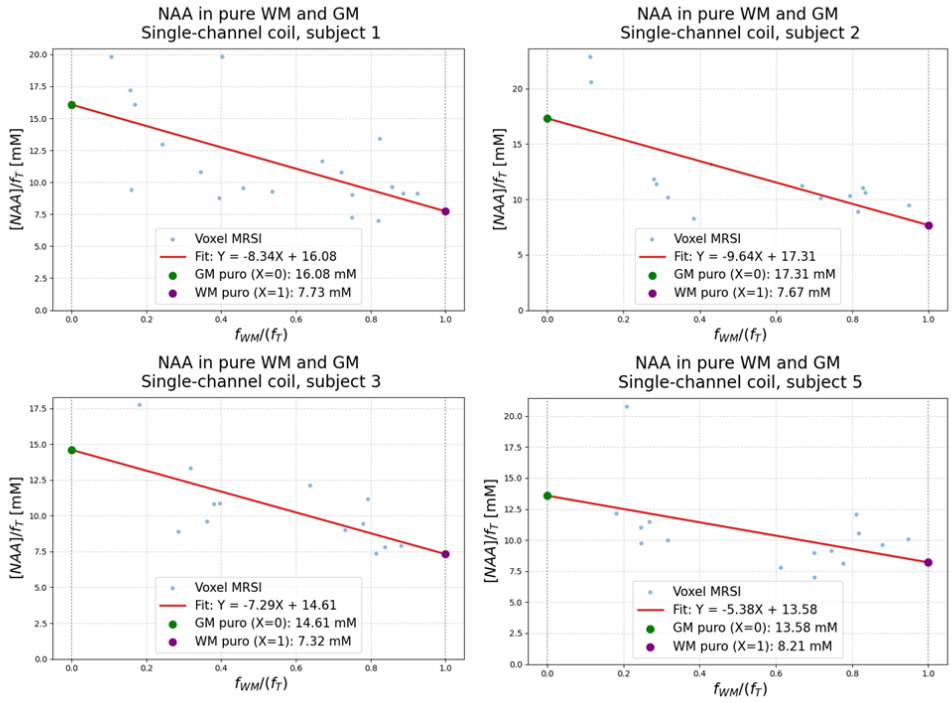

Figure 5.9: Linear fitting of C_T/f_T as a function of f_{WM}/f_T according to Equation 4.5. Data were acquired for each subject using a single-channel coil. Since the quantification of NAA concentration was reliable for only a single voxel, the linear fit could not be assessed for Subject 4.

Chapter 6

Discussion

This thesis has demonstrated that working on the impact of parameter optimisation and coil comparison using first phantom and then in vivo data. Indeed, at the end of this work it was possible to give some recommendation for future in vivo in patients acquisition of MRSI in the brain. Scan times were as short as 6 minutes for a single CSI slice position. The first part of this study aimed to optimize scanner parameters to enable 2D MRSI slice acquisition balancing high SNR, clinically feasible acquisition times, and precise brain metabolite estimation.

6.1 In phantom optimization

Twenty-six scans were performed on a GE "Braino" phantom, systematically varying WS methods, TR, acceleration factor, shimming, chemical shift direction, and RF pulse shape.
The impact of the different WS methods evaluated (excitation, CHESS, and MOIST) is shown in Table 5.17 and 5.2. These results clearly show that varying the WS method leads to statistically significant differences in SNR and NAA concentration distributions: the excitation method yielded the highest average SNR, whereas CHESS provided the highest average NAA concentration in a.u. (closest to the nominal phantom value). To ensure a more reliable estimation across all metabolite concentrations, the method yielding the highest SNR was preferred (reflecting lower noise levels, as SNR was evaluated on the NAA peak). Nonetheless, for the in vivo optimization, it was decided to re-test the WS methods by comparing excitation and MOIST, as MOIST is expected to be more robust against B_1 inhomogeneities.
The second parameter investigated was the impact of TR on SNR and ac-

quisition time: the corresponding boxplot in Figure 5.4 clearly shows that TR = 1000 ms is the only setting that prevents complete recovery of the NAA signal, leading to an underestimation of the NAA concentration compared to the other three values. As shown in Table 5.3, TR = 1500 ms yielded the highest SNR per unit time (or highest SNR with the shortest acquisition time), making it the optimal TR chosen for subsequent steps in this study.
Acceleration is one of the parameters with the greatest impact on scan time, halving it when enabled (phantom acquisition time decreased from 2:43 min to 1:22 min). In addition to comparing SENSE ON versus OFF, the combination of SENSE ON with NSA = 2 was assessed, resulting in a very short acquisition time (2:37 min) comparable to SENSE OFF. As reported in Table 5.5 and 5.6, enabling acceleration yielded no statistically significant differences in SNR or NAA concentration distributions in a.u., suggesting that acceleration could effectively reduce scan time without substantial signal loss. However, when evaluating the absolute NAA concentration distribution in mM, as in reported in Table 5.7, the SENSE OFF acquisition yielded a mean concentration statistically different from the accelerated conditions and considerably closer to the nominal phantom value (mean NAA concentration = 10,9 mM vs. nominal concentration = 12,5 mM). This suggests that while relative peak ratios remained stable, SENSE reconstruction may introduce inaccuracies during the unsuppressed water reference normalization, leading to an underestimation of absolute concentrations in mM despite yielding comparable relative values in a.u.
The importance of disabling SENSE was confirmed in the fourth part of this optimization, where the effect of acceleration was evaluated in combination with setting an automatic versus manually selected shim volume, and the largest increase in SNR was achieved by setting shimming to Pb_volume and SENSE to OFF. Absolute NAA concentration estimation in mM was likewise improved with Pb_volume and SENSE OFF, resulting in a mean concentration of 10,9 mM compared to 7,4 mM. Adjusting only the shimming parameter from Pb_auto to Pb_volume resulted in an increased SNR, but no statistically significant difference in NAA concentration (Table 5.10). Therefore, this substantial increase in SNR justified setting SENSE to OFF and manually defining the shimming volume for the subsequent steps of this study. Nevertheless, this configuration was re-evaluated in vivo to determine whether the longer acquisition time remains clinically feasible and justified.
Regarding the RF pulse shape, as shown in Tables 5.11 and 5.12, the "Sharp" pulse profile yielded the highest estimated NAA concentration, whereas the highest average SNR was achieved using the "Classic-Long" pulse. For the subsequent stages of this study, the "Sharp" pulse was selected: its steeper excitation profile minimizes chemical shift displacement artifacts at the VOI

boundaries, thereby ensuring more accurate voxel localization and nominal concentration quantification, at the expense of a trade-off in peak SNR.
In addition to the parameters described above, the chemical shift direction was also varied - not for optimization purposes, but to investigate whether the darker region observed in the SNR heatmaps across all acquisitions was caused by coil malfunction or by the spatial displacement of the NAA resonance relative to the VOI (whose position is prescribed based on the water resonance frequency). This low-SNR region is illustrated in Figure 5.2, which also shows how its position shifts across different sides of the map when altering the chemical shift direction. This confirmed that the SNR imbalance was not due to faulty coil elements in the multi-channel array, but rather to the chemical shift displacement artifact.
Lastly, the multi-channel and single-channel coils were compared on the phantom by performing two acquisitions with the multi-channel coil (varying the shimming parameter from Pb_auto to Pb_volume) and repeating the same protocol with the single-channel coil. The results are summarized in Tables 5.13 and 5.14. Regarding SNR, switching coils resulted in statistically significant differences ($p < 0,05$), demonstrating a substantial SNR gain with the multi-channel setup (SNR multi/single-channel = 17,8/9,4 a.u. with Pb_auto, and 20,6/17,1 a.u. with Pb_volume). Furthermore, manually defining the shimming volume yielded a consistent improvement in average SNR over automatic shimming, an effect that proved even more critical for the single-channel coil setup (single-channel SNR = 9,4 a.u. with automatic shimming vs. 17,1 a.u. with manual shimming volume selection).
Regarding NAA quantification, the mean NAA concentration was closer to the nominal phantom value (12,5 mM) in the multi-channel acquisition (10,9 mM) compared to the single-channel one. However, no statistically significant difference was observed between multi- and single-channel NAA concentration estimates ($p = 0,28$) when the shimming parameter was set to Pb_volume, confirming the substantial impact of shimming on single-channel coil performance. On the other hand, the standard deviation (SD) of the NAA concentration distribution was lower in both single-channel acquisitions (as shown in the final boxplot of Figure 5.4), indicating a more homogeneous NAA concentration estimate and suggesting that single-channel coils could inherently provide a more homogeneous B_1 field distribution across the FOV compared to surface coil arrays, leading to more uniform spatial metabolite quantification. This aspect was further investigated in the *in vivo* comparison; nevertheless, in terms of overall SNR, the multi-channel coil demonstrated superior performance at this stage of the study.
Direct comparisons of these optimization results with existing literature are limited, as systematic multi-parameter optimization studies evaluating WS tech-

niques, TR, shimming performance, RF pulse shapes, and SENSE simultaneously within a single 2D MRSI protocol remain scarce. Instead, published studies predominantly investigate these parameters independently or focus on dedicated technological developments, though certain isolated findings (such as the expected decrease in SNR when employing SENSE [24]) are well-aligned with the observations in this study.

6.2 In vivo parameter optimization

In this section of the study, a subset of the parameters was re-evaluated in vivo by analysing the SNR distributions within the VOI to validate the findings previously obtained on the phantom. First, shimming and SENSE acceleration were re-tested on a single subject to confirm the results, as they were among the parameters that yielded the greatest SNR improvement in phantom, obtaining the results summarized in Table 5.15. Setting SENSE OFF or keeping SENSE ON with 2 NSA meant that the acquisition time increased to approximately 7 min, which is clinically acceptable. Both acquisitions had similar SNR. However, because the unaccelerated acquisition demonstrated consistently higher SNR both in phantom and in vivo, SENSE OFF was chosen as the optimal setting for the subsequent protocol. Finally, the in vivo scan on this subject confirmed the benefit of manual shimming volume selection over the automatic preset with improved in vivo SNR from 22,6 a.u. to 25,1 a.u.
In another subject, the water suppression method was re-tested by comparing excitation and MOIST. As previously stated, the goal was to assess MOIST performance in vivo, as it is expected to provide greater robustness against B_1 inhomogeneities, whereas excitation had yielded the highest average SNR in the phantom acquisitions. In the in vivo evaluation (results in Table 5.17), no statistically significant differences (p-value = 0,43) were observed between the mean SNRs of the two methods; consequently, MOIST was selected as the default water suppression technique for the optimized protocol.
An additional parameter evaluated in vivo was the reconstructed voxel size. The purpose was to investigate whether reconstructing voxels with smaller nominal dimensions could enhance spatial resolution without an excessive penalty in SNR or data accuracy. For the final optimized protocol, the reconstructed voxel size was matched to the acquisition dimensions; nonetheless, these results demonstrated that higher spatial resolution is feasible at the expense of longer scan times while maintaining acceptable SNR levels.
The final acquisitions in this in vivo optimization served, as in the phantom experiments, as a preview for the coil comparison in the latter part of the study.

6.3 In vivo coil comparison

The final part of this work addresses the evaluation of coil performance in measuring neurotransmitter concentrations, comparing a dedicated ^{1}H multi-channel head coil against the ^{1}H channel of a dual-tuned ^{1}H/^{23}Na coil.
To this end, five subjects were scanned with both coils following the pipeline described in Section 4.5. For each subject, one MRSI slice per coil was acquired, positioned in the white matter (WM) as shown in Figure 4.2, using the scanner parameters determined from the optimization phase of this study (Table 4.3).
As described in Section 5.3.1 and detailed in Table 5.19, evaluating the SNR distribution within the VOI across subjects demonstrates that the multi-channel head coil systematically outperforms its single-channel counterpart.

Regarding the quantification of NAA concentration, a distinct data analysis pipeline was required for the in vivo acquisitions. Due to voxel tissue heterogeneity, namely, varying volume fractions of WM and GM across the VOI, the NAA concentration was not spatially uniform. Moreover as the subject needed to be repositions between the two coils acquisitions, the matching of the spatial position of the VOI may be slightly different between the two. Consequently, NAA concentrations across the VOI could not simply be pooled into a single global distribution, as was done for the phantom scans. Instead, tissue segmentation was performed to extract the specific WM and GM volume fractions for each voxel, as detailed in Section 4.6.3. To obtain a representative NAA value for each acquisition, the concentration in pure WM was estimated via linear regression based on Equation 4.3, which leads to the model in Equation 4.5.
The regression coefficients of determination were low (R^2 ranging between 0,097 and 0,21): as illustrated in Figure 5.8, although NAA concentration decreases with increasing WM fraction (consistent with physiological expectations, as GM exhibits higher NAA levels) the data exhibit substantial scatter around the regression line. This dispersion may account for the absolute NAA concentrations obtained with the multi-channel coil (ranging from $8,7 \pm 1,4$ mM to $13,6 \pm 1,1$ mM), which appear systematically overestimated compared to the expected physiological value in WM ($\sim$ 7 mM). More accurate absolute quantification and linear calibration would require incorporating T_1/T_2 relaxation and CSF partial volume corrections. Although coil sensitivity profile adjustments are recommended in multi-channel acquisitions to prevent overestimation [25], our phantom data showed no such bias. This indicates that additional corrections are primarily needed within the in vivo linear quantification model.

For the single-channel acquisitions, data for Subject 4 could not be evaluated: TARQUIN yielded an acceptable fit (SD% < 20) in only a single voxel within the VOI, possibly due to either subject's motion or a bad shim. For the remaining subjects, the number of retained voxels was substantially lower than in the multi-channel acquisitions, indicating that over half of the spectra were rejected, as depicted in Figure 5.7. Despite the smaller sample size, the estimated concentrations were closer to physiological expectations, ranging from $7,3 \pm 1,3$ mM to $7,7 \pm 1,4$ mM, with higher variance explained by the model (R^2 between 0,36 and 0,42; Table 5.21, Figure 5.9).Consequently, while the single-channel acquisitions yielded regression estimates closer to literature values and higher R^2 values despite a reduced number of usable voxels (notably, fitting the identical subset of voxels in the multi-channel data failed across all five subjects), they suffered from severe spectral quality degradation and data loss.To formally compare the two coils, statistical comparisons were performed (Table 5.22). The $p\text{-value}_{\text{coil}}$ values indicate that, although single-channel estimates were closer to expected values, the difference in pure WM NAA concentration between the two coils did not reach statistical significance for most subjects (p ranging from 0,07 to 0,17), with Subject 1 being the sole exception. Furthermore, the interaction term ($p\text{-value}_{\text{int}}$) showed no significant difference in regression slopes between coils (p ranging from 0,43 to 0,85), confirming that both setups captured a consistent rate of NAA decrease as a function of WM fraction.In summary, the single-channel coil yielded WM NAA concentration estimates closer to physiological literature values, whereas the multi-channel coil produced systematic overestimations. However, ordinary least squares (OLS) comparison demonstrated that these differences were largely non-significant. Crucially, the multi-channel coil provided superior spectral quality and SNR, enabling robust spectral fitting across nearly the entire VOI, whereas the single-channel coil suffered extensive voxel exclusion. Moreover, the multi-channel coil NAA evaluation in WM demonstrated greater inter-subject variance (SD= $1,9$ vs. $0,37$ mM), suggesting a higher sensitivity to biological variation across individuals, a critical property for clinical studies comparing healthy controls to pathological cohorts.

Chapter 7

Conclusions

This pilot study establishes an optimized 2D MRSI protocol that balances high SNR with a clinically feasible scan time, aiming to ensure accurate quantification of neurometabolites in brain slices. Following phantom evaluations that systematically assessed scanner parameters and their impact on acquisition time, SNR, and NAA quantification, the resulting optimal protocol was defined as: WS = Excitation, TR = 1500 ms, SENSE = OFF, manual shimming volume selection (Shimming = Pb-volume), and RF pulse = Sharp. In phantom measurements, this protocol yielded the highest SNR ($20,6 \pm 4,5$ a.u.) within a scan time of 2,43 minutes. It is worth noting that if scan time must be prioritized over SNR efficiency, such as in prospective 3D MRSI acquisitions, activating SENSE (acceleration factor 2×2) reduces the acquisition time to 1,22 minutes, at the cost of an SNR decrease of approximately 14% .

The performance of this optimized protocol was subsequently confirmed in vivo, with a single modification to the water suppression technique: MOIST was preferred over Excitation due to its theoretical greater robustness against B_1 field inhomogeneities. Consistently, though, in vivo metabolite quantification showed no statistically significant difference between Excitation and MOIST ($p = 0,43$).

The final part of this study compared the performance of two RF coils in quantifying cerebral neurometabolite concentrations: a dedicated state-of-the-art ^{1}H multi-channel head coil versus the single-channel ^{1}H element of a dual-tuned ^{1}H/^{23}Na coil. The comparative assessment was conducted in vivo on five HCs using the previously optimized scanning parameters (summarized in Table 4.3). A 2D MRSI sequence of 6 minutes was performed with each coil, remaining well within a clinically feasible acquisition window. The results clearly demonstrated the superior data quality provided by the multi-channel coil. Specifically, the multi-channel coil achieved an average SNR of $25,5 \pm 1,2$ a.u., compared to $11,2 \pm 2,6$ a.u. for the single-channel coil, corresponding to a

128% increase in SNR. When evaluating NAA concentration in WM, the multi-channel coil exhibited higher inter-subject variance ($1,9$ vs. $0,37$), alongside a substantially higher number of reliably fitted voxels in TARQUIN (46 vs. 12). The higher inter-subject variance in WM NAA obtained with the multi-channel coil most probably reflects biological heterogeneity across subjects, which was otherwise obscured by the low sensitivity and limited spectral reliability of the single-channel setup. Capturing this physiological variance is critical for future clinical studies comparing healthy controls to pathological cohorts.

In a broader perspective, while MRSI represents the primary non-invasive technique available to map regional neurometabolite concentrations in the human brain, its clinical integration remains limited. This is largely driven by technical and methodological barriers, including low SNR, limited spatial resolution, long acquisition times and lack of standardized acquisition protocols. By addressing these challenges this study has provided a protocol for the 2D-MRSI acquisition in the WM region of the brain, laying the groundwork for further MRSI studies: further investigations would focus on spatial resolution, 3D spectroscopic imaging, and applications targeting specific low-concentration metabolites, while future implementation of this protocol would involve clinical studies measuring brain metabolites as biomarkers to study neurodevelopment or neurological disorders.

Bibliography

[1] A Robin and DE GRAAF. *IN VIVO NMR SPECTROSCOPY; PRINCIPLES AND TECHNIQUES*. JOHN WILEY., 2007.

[2] Robert W. Brown, Yu-Chung N. Cheng, E. Mark Haacke, Michael R. Thompson, and Ramesh Venkatesan. *Magnetic resonance imaging : physical principles and sequence design*. John Wiley Sons, Incorporated, Hoboken, New Jersey, second edition. edition, 2014 - 2014.

[3] Steven M Wright and Lawrence L Wald. Theory and application of array coils in mr spectroscopy. *NMR in Biomedicine: An International Journal Devoted to the Development and Application of Magnetic Resonance In Vivo*, 10(8):394–410, 1997.

[4] Petra Hnilicová, Michal Považan, Bernhard Strasser, Ovidiu C. Andronesi, Martin Gajdošík, Ulrike Dydak, Jozef Ukropec, Dušan Dobrota, Siegfried Trattnig, and Wolfgang Bogner. Spatial variability and reproducibility of gaba-edited mega-laser 3d-mrsi in the brain at 3t. *NMR in Biomedicine*, 29(11):1656–1665, 2016.

[5] Wolfgang Bogner, Borjan Gagoski, Aaron T. Hess, Himanshu Bhat, M. Dylan Tisdall, Andre J.W. van der Kouwe, Bernhard Strasser, Małgorzata Marjańska, Siegfried Trattnig, Ellen Grant, Bruce Rosen, and Ovidiu C. Andronesi. 3d gaba imaging with real-time motion correction, shim update and reacquisition of adiabatic spiral mrsi. *NeuroImage*, 103:290–302, 2014.

[6] Helge J. Zöllner, Dillip K. Senapati, İpek Özdemir, Kimberly L. Chan, Georg Oeltzschner, Doris D. M. Lin, and Peter B. Barker. Reproducibility of metabolic mapping using 2d multi-slice short-te and gaba-edited spin-echo mrsi at 3t in a single protocol. *NMR in Biomedicine*, 39(1):e70175, 2026. e70175 NBM-25-0230.

[7] Georgios Paslakis, Frank Träber, Jens Roberz, Wolfgang Block, and Frank Jessen. N-acetyl-aspartate (naa) as a correlate of pharmacological treat-

ment in psychiatric disorders: A systematic review. *European Neuropsychopharmacology*, 24(10):1659–1675, 2014.

[8] Saurabh Jain, Diana M. Sima, Faezeh Sanaei Nezhad, Gilbert Hangel, Wolfgang Bogner, Stephen Williams, Sabine Van Huffel, Frederik Maes, and Dirk Smeets. Patch-based super-resolution of mr spectroscopic images: Application to multiple sclerosis. *Frontiers in Neuroscience*, Volume 11 - 2017, 2017.

[9] Jerrold T. Bushberg. *The *essential physics of medical imaging / Jerrold T. Bushberg ... [et al.].* Wolters Kluwer, Philadelphia [etc, 4. ed. edition, 2021.

[10] Axel Haase, Jens Frahm, Wolfgang Hanicke, and Dietmar Matthaei. 1h nmr chemical shift selective (chess) imaging. *Physics in Medicine & Biology*, 30(4):341–344, 1985.

[11] Paul de Heer, Maurice B. Bizino, Hildo J. Lamb, and Andrew G. Webb. Parameter optimization for reproducible cardiac 1h-mr spectroscopy at 3 tesla. *Journal of Magnetic Resonance Imaging*, 44(5):1151–1158, 2016.

[12] Klaas P Pruessmann, Markus Weiger, Markus B Scheidegger, and Peter Boesiger. Sense: sensitivity encoding for fast mri. *Magnetic Resonance in Medicine: An Official Journal of the International Society for Magnetic Resonance in Medicine*, 42(5):952–962, 1999.

[13] Eugene Ozhinsky, Daniel B. Vigneron, and Sarah J. Nelson. Improved spatial coverage for brain 3d press mrsi by automatic placement of outer-volume suppression saturation bands. *Journal of Magnetic Resonance Imaging*, 33(4):792–802, 2011.

[14] Val M Runge and Johannes T Heverhagen. Number of averages. In *The Physics of Clinical MR Taught Through Images*, pages 46–47. Springer, 2022.

[15] Maryam Vareth, Janine M Lupo, Peder EZ Larson, and Sarah J Nelson. A comparison of coil combination strategies in 3d multi-channel mrsi reconstruction for patients with brain tumors. *NMR in Biomedicine*, 31(11):e3929, 2018.

[16] Paul A Bottomley et al. Spatial localization in nmr spectroscopy in vivo. *Ann NY Acad Sci*, 508(1):333–348, 1987.

[17] Noam Soreni, Michael D Noseworthy, Toni Cormier, Wendy K Oakden, Sonya Bells, and Russell Schachar. Intraindividual variability of striatal 1h-mrs brain metabolite measurements at 3 t. *Magnetic resonance imaging*, 24(2):187–194, 2006.

[18] Martin Wilson, Greg Reynolds, Risto A Kauppinen, Theodoros N Arvanitis, and Andrew C Peet. A constrained least-squares approach to the automated quantitation of in vivo 1h magnetic resonance spectroscopy data. *Magnetic resonance in medicine*, 65(1):1–12, 2011.

[19] Martin Wilson. *TARQUIN User Guide*. SourceForge, 2020. Accessed: 2026-08-11.

[20] Xiangrui Li, Paul S Morgan, John Ashburner, Jolinda Smith, and Christopher Rorden. The first step for neuroimaging data analysis: Dicom to nifti conversion. *Journal of neuroscience methods*, 264:47–56, 2016.

[21] M Jorge Cardoso, Marc Modat, Robin Wolz, Andrew Melbourne, David Cash, Daniel Rueckert, and Sebastien Ourselin. Geodesic information flows: spatially-variant graphs and their application to segmentation and fusion. *IEEE transactions on medical imaging*, 34(9):1976–1988, 2015.

[22] M. Jorge Cardoso, Matthew J. Clarkson, Marc Modat, and Sébastien Ourselin. NiftySeg: Open-source software for medical image segmentation, parcellation and label fusion. `https://github.com/KCL-BMEIS/NiftySeg`, 2012.

[23] Marc Modat, Gerard R Ridgway, Zeike A Taylor, Manja Lehmann, Josephine Barnes, David J Hawkes, Nick C Fox, and Sébastien Ourselin. Fast free-form deformation using graphics processing units. *Computer methods and programs in biomedicine*, 98(3):278–284, 2010.

[24] Oun Al-Iedani, Jeannette Lechner-Scott, Karen Ribbons, and Saadallah Ramadan. Fast magnetic resonance spectroscopic imaging techniques in human brain-applications in multiple sclerosis. *Journal of biomedical science*, 24(1):17, 2017.

[25] Brian J. Soher, Peter C. M. van Zijl, Jeffrey H. Duyn, and Peter B. Barker. Quantitative proton mr spectroscopic imaging of the human brain. *Magnetic Resonance in Medicine*, 35(3):356–363, 1996.